



# Three-dimensional distribution of permafrost and responses to increasing air temperatures in the head waters of the Yellow River in High Asia

Aili Sun <sup>a,b</sup>, Jian Zhou <sup>c</sup>, Zhongbo Yu <sup>a,b,\*</sup>, Huijun Jin <sup>c</sup>, Yu Sheng <sup>c</sup>, Chuanguo Yang <sup>a,b</sup>

<sup>a</sup> State Key Laboratory of Hydrology-Water Resources and Hydraulic Engineering, Hohai University, Nanjing 210098, China

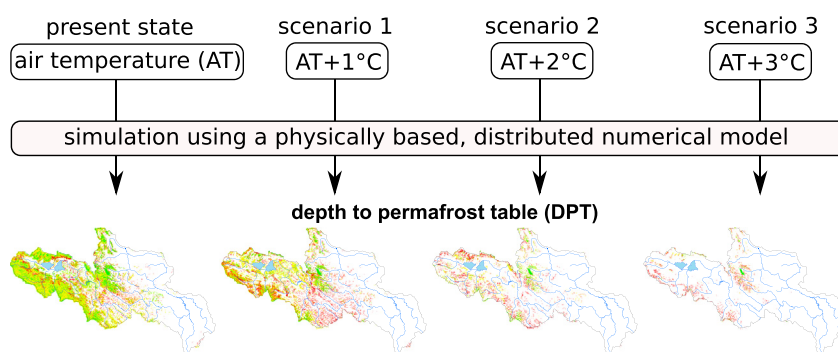
<sup>b</sup> College of Hydrology and Water Resources, Hohai University, Nanjing 210098, China

<sup>c</sup> Cold and Arid Regions Environmental and Engineering Research Institute, Chinese Academy of Sciences, Lanzhou, Gansu 730000, China

## HIGHLIGHTS

- To know the fine 3D distribution of permafrost at the basin scale is still difficult.
- A process-based, distributed numerical model was applied against warming climate.
- The permafrost will degrade severely with the area decreasing rate as 36%/°C.
- The sensitivity of permafrost to warming is higher in low land areas than mountains.

## GRAPHICAL ABSTRACT



## ARTICLE INFO

### Article history:

Received 20 September 2018

Received in revised form 18 December 2018

Accepted 7 February 2019

Available online 8 February 2019

Editor: Ouyang Wei

### Keywords:

3D distribution

Depth-to-permafrost table

Ground temperature

Air temperature

Permafrost

Climate change

## ABSTRACT

Fine-scale three-dimensional (3D) permafrost distributions at the basin scale are currently lacking. They are needed to monitor climate and ecosystem change and for the maintenance of infrastructure in cold regions. This paper determined the horizontal and vertical distributions of permafrost and its quantitative responses to climate warming in the High Asia region by constructing a quasi-3D model that couples heat transfer and water movement and is forced by spatially-interpolated air temperatures using an elevation-dependent regression method. Four air temperature scenarios were considered: the present state and air temperature increases of 1, 2 and 3 °C. A fine-scale permafrost map was constructed. The map considered taliks and local factors including elevation, slope and aspect, and agreed well with field observations. Permafrost will experience severe degradation with climate warming, with decreases in area of 36% per degree increase in air temperature, increases in the depth-to-permafrost table of 2.67 m per degree increase in air temperature, and increases in 15 m-depth ground temperatures of 1.25 °C per degree increase in air temperature. Permafrost is more vulnerable in and beside river valleys than in high mountains, and on sunny rather than shady slopes. These results provide an effective reference for permafrost prediction and infrastructure and ecosystem management in cold regions affected by global warming.

© 2019 Elsevier B.V. All rights reserved.

## 1. Introduction

In the headwaters of the Yellow River in the High Asia region, permafrost degradation due to climate change has been of increasing

\* Corresponding author at: State Key Laboratory of Hydrology-Water Resources and Hydraulic Engineering, Hohai University, Nanjing 210098, China.

E-mail address: [zyu@hhu.edu.cn](mailto:zyu@hhu.edu.cn) (Z. Yu).

interest to researchers. It can contribute to the degradation of wetlands (Walvoord et al., 2012; Zhang et al., 2006b), infrastructure (Heginbottom, 2002) and grasslands, and cause farmland desertification (Bring et al., 2016; Cannon et al., 2014; Nelson et al., 2001; Zeng and Feng, 2007), water resource crises and the drying up of rivers (Huang and Zhou, 2012; Wang et al., 2000; Wang and Zhou, 1998; Wang and Cheng, 2001; Yang et al., 2004). The distribution of permafrost and its changes have been monitored over the last two decades by a range of projects, such as the Swiss National Research Project 31 (NFP31) the *Climate Change and Natural Hazard* project (Lugon and Monbaron, 1998; Haeblerli et al., 1999), the European Union's *Permafrost and Climate in Europe* (PACE) project (Harris et al., 2001; Riseborough et al., 2008), the *Climate and Cryosphere* (CliC) Project's *Science and Coordination Plan and the Coordinated Energy and Water Cycle Observations Project* (CEOP), which is part of the *Global Energy and Water Cycle Experiment* (GEWEX; Williams, 2010). The High Asia region is a unique area of mid-to-low latitudes with different types of permafrost. The region is regarded as a driver and amplifier of climate change in China (Feng and Tang, 1998; Pan et al., 1995a, 1995b; Pan and Li, 1996), which makes it a suitable place to study permafrost changes and the impacts of climate change (Cuo et al., 2015; Li et al., 2016b; Liu and Jiang, 2016). It has been reported that, during the last 40 years, the surface air temperature in cold regions has increased by approximately twice the global average (Lemke et al., 2007). According to the results of the *Representative Concentration Pathway 4.5* (RCP4.5), which is based on 22 climate models from the *Coupled Model Intercomparison Project Phase 5* (CMIP5), the surface air temperature in China in 2081–2100 will have increased by  $2.6 \pm 0.8$  °C relative to 1986–2005 temperatures (Tian et al., 2015). Permafrost degradation has been shown to be much more sensitive to conditions of severe climate warming in the periphery of the High Asia region than in its interior (Jin et al., 2007). To comprehensively evaluate the region's responses to climate change, scientists have focused on spatial and temporal permafrost mapping.

Permafrost change has been investigated by drilling boreholes to precisely map its distribution and depth. Measured soil temperatures from 190 boreholes drilled since the 1960s show permafrost thicknesses ranging from 10 to 300 m along the Qinghai-Tibet Highway/Railway (Wu et al., 2010). The active layer thickness (ALT) of permafrost in this area increased by 10–40 cm from 1995 to 2004 (Wu and Zhang, 2010). The mean annual ground temperature (MAGT) of permafrost is between  $-1$ – $0$  °C in boreholes along State Road 214 (Sheng et al., 2015). In the Yellow River source area, the temperatures at the top of the permafrost (TTOP) are  $-1.9$  °C,  $-0.9$  °C,  $-0.4$  °C and  $1.1$  °C at the Chalaping (CLP), Gyaring Lake (ZLH), Maduo Town site (MDX) and Ngoring Lake (ELH) study sites (Luo et al., 2014a). However, due to the severe natural environment of these areas, soil temperature measurement in drilled boreholes is difficult and few long-term monitoring sites exist (Romanovsky et al., 2010). Measurements taken over a limited time range can indicate short-term changes in soil or ground temperatures, and only at certain points (Cheng and Wu, 2007; Jin et al., 2006; Wu and Zhang, 2010). This is an obstacle to the understanding of large-scale spatial and temporal trends in permafrost degradation.

To overcome this limitation, many conceptual, empirical and numerical models (Briggs et al., 2014; Jiang et al., 2012; McKenzie and Voss, 2013; Qin et al., 2017; Riseborough et al., 2008) have been utilised forced by results of general circulation models (GCMs) (Koven et al., 2012; Ni, 2000; Zhang et al., 2013b; Zhang and Wu, 2012) to estimate historical and future permafrost degradation rates around the world. Conceptual and empirical models, such as the TTOP model (Smith and Riseborough, 1996), Stefan model, and Kudryavtsev model (Kudryavtsev et al., 1974, 1977) require limited data. However, these models produce coarser resolutions than process-based models, such as the Northern Ecosystem Soil Temperature (NEST) model (Zhang et al., 2006a) and Geophysical Institute Permafrost Laboratory model

of University of Alaska Fairbanks (UAF-GIPL 2.0; Marchenko, 2008), which require large amounts of spatial data. An empirical model of MAGTs was regressed against elevation and altitude based on about 20 years of borehole soil temperature data. Results were used to map the High Asia region's permafrost distribution (Nan et al., 2002). However, conceptual and empirical models usually applied in large-scale permafrost mapping do not provide reasonable distributions under the impacts of certain local factors (Cheng, 2004) that have been shown to have clear impacts on ground temperatures at the north edge of the High Asia region (Sun et al., 2010). In addition, high heterogeneity and complexity in the actual distribution of permafrost may pose considerable scaling challenges (Walvoord and Kurylyk, 2016). In order to tackle this problem, a numerical geomorphology-based eco-hydrological model (GBEHM) was applied to the headwaters of the Yellow River in one study (Qin et al., 2017). This process-based numerical model has shown excellent performance in simulating active layer thickness (ALT) and permafrost temperatures (Zhang et al., 1996; Zhang and Stamnes, 1998). At local scales, three-dimensional (3D) estimates of soil temperature have been made using the NEST model (Kurylyk et al., 2016); the topography and energy-balance model (TEABAL; Noetzi et al., 2007); a new, fine-scale, fully-coupled, surface/subsurface thermal hydrology model based on ATS (Arctic Terrestrial Simulator; Painter et al., 2016); and the combined NEST and SUTRA (Saturated Subsurface Model) model (Kurylyk et al., 2016). Numerical modelling has been applied to smaller regions (Heginbottom et al., 1992) with areas of  $<5$  km<sup>2</sup> and resolutions smaller than 20 m. However, such regional-scale models are inadequate for assessing the effects of permafrost degradation due to global warming on water resources and ecosystems. Larger scales, such as basins or watersheds that are susceptible to social and economic activities, are of great importance for comprehensively understanding permafrost distributions and their responses to global warming. It is difficult to obtain high resolution permafrost distributions at the basin scale.

To overcome this situation, this study focused on the 3D distribution of permafrost and its response to increasing air temperatures at the basin scale on the edge of the High Asia region. The water balance simulation model (WaSiM) is a process-based, distributed numerical model. It was applied to the headwaters of the Yellow River (HWYR). This study aimed to understand the equilibrium ground thermal states estimated from transient results under various climate warming scenarios. The objectives of this research were to: (a) evaluate the accuracy of simulations based on observation, (b) simulate the spatial distribution of the depth-to-permafrost table (DPT) and ground temperatures at 15 m depth, and (c) analyse and quantify permafrost changes in both horizontal and vertical aspects under various scenarios of air temperature increase.

## 2. Study area and data

### 2.1. The study area

This study focused on a permafrost fragile watershed: the headwaters of the Yellow River (HWYR), which lies in the northeastern region of High Asia (Fig. 1). The study area was located between  $95^{\circ}50'$ – $103^{\circ}30'$  E and  $32^{\circ}20'$ – $36^{\circ}10'$  N. The HWYR, including its drainage area, is about 123,009 km<sup>2</sup> in area and contains the outlet Tangnaihai hydrological gauge (TNH). The HWYR area comprises 12% of the Yellow River. The HWYR, also known as the TNH basin, has two large lakes, Gyaring Lake and Ngoring Lake. The elevation in the HWYR varies from 3000 to 6253 m above sea level, with the highest point being the Amne Machin Mountain (Fig. 1). The Buqing Mountain and Bayan Har Mountain form the northern and southern edges of the basin, respectively. The Amne Machin Mountain stretches from northwest to the centre of the basin, making the main river a U-turn at Roige Plain (Fig. 1). With the semi-humid climate of the HWYR, the annual mean air temperature varies between  $-14$  and  $4.5$  °C from the southwest to

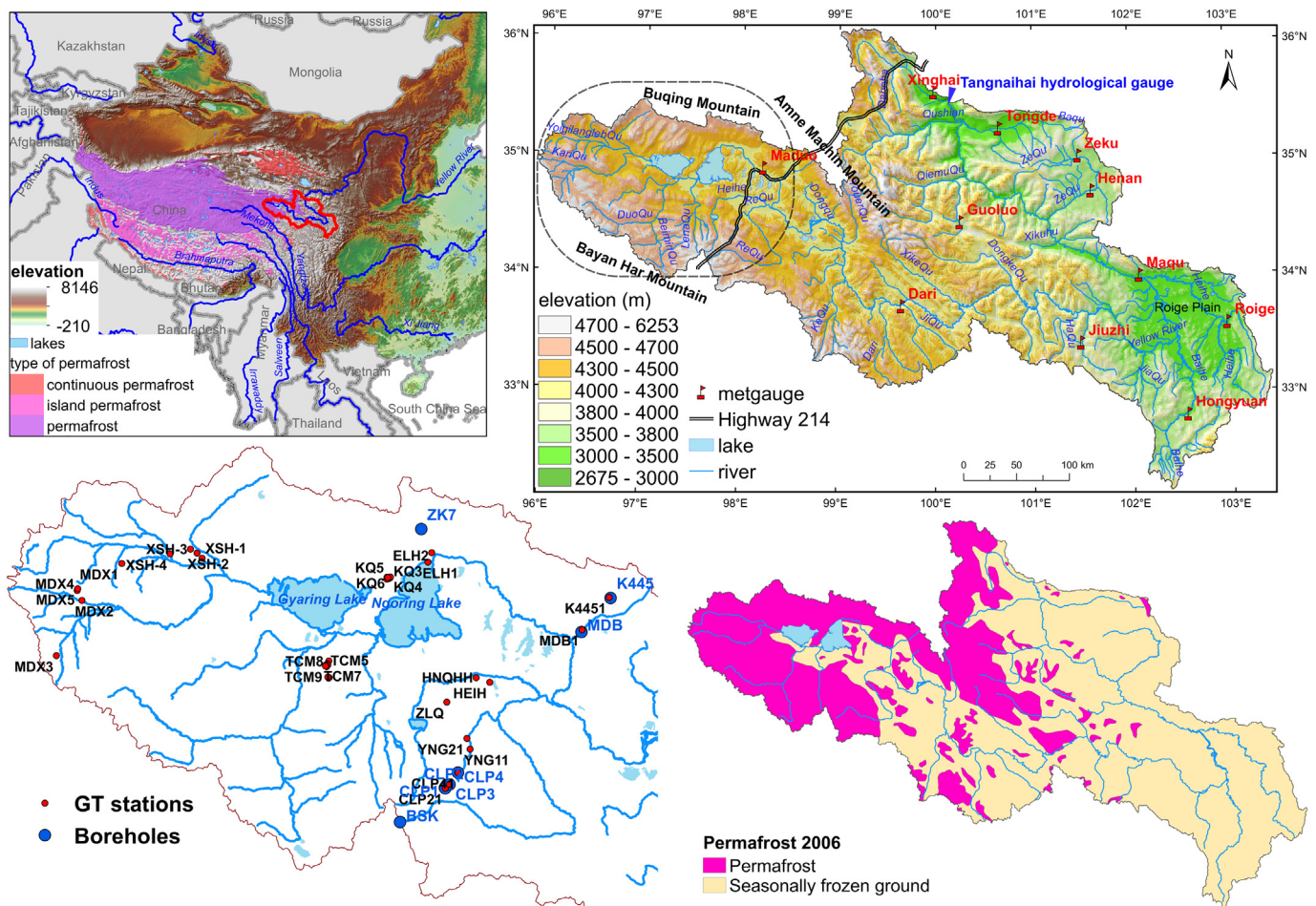


**Fig. 1.** The location of the headwaters of the Yellow River (HWYR), elevation, drainage system, lakes, meteorological gauges (metgauge in figure), ground temperature stations (GT stations, red small point with black text label), boreholes and ALT stations (both in blue large point with blue text label), Permafrost map made in 2006.

northeast, according to meteorological observations from 1979 to 2014. Annual mean precipitation varies from 250 to 770 mm, 75–90% of which occurs from June to September due to the effect of southwest monsoons in the Bay of Bengal. Fig. 1 shows boreholes and stations for monitoring ground temperature at 15 m depth (GT) and active layer thickness.

According to current mapping of frozen ground in the region, which is shown in Fig. 1 (Wang, 2006), permafrost comprises approximately 34% of the whole watershed. The rest of the watershed is comprised of seasonally frozen ground. The existence of three types of ground in the HWYR may be due to continuous degradation. Therefore, this watershed area could be highly sensitive to permafrost degradation due to climate change (Qin et al., 2017; Yang et al., 2013). State Road 214 stretches across permafrost areas of the HWYR (Fig. 1). Hence, study and simulation of the permafrost distribution in this area is of great importance in terms of global climate change impacts and the development of ecosystems and infrastructure.

## 2.2. Data

Geographical, soil, land cover and climatic forcing data from 2010 to 2012 were used to drive the model. Digital elevation model data was taken from the US Geological Survey's (USGS) GTOPO30 dataset. This data had an original resolution of 30 arc sec, and was resampled to a 1 km cell size resolution for the study area. A 1:100,000 scale land-use map (Fig. 2(a)) was provided by the Environmental and Ecological Science Data Centre for West China (WestDC; Liu et al., 2003). This

map was derived from remote sensing images from the Landsat 1–5 Multispectral Scanner (MSS), 4–5 Thematic Mapper (TM) and 7 Enhanced Thematic Mapper Plus (ETM+). The map shows that grassland comprises >70% of the total study area. Wetlands are mainly distributed along the Roige Plain and around the Zeku meteorological station (Fig. 1). Vegetation parameters for different land cover types were carefully adjusted from the coupled different sub-models (COUPMODEL) settings (Jansson and Karlberg, 2001) to be suitable for the HWYR. Soil data (Fig. 2(b)) was taken from the Soil Map of China 1:1 Million scale, which is based on data from the office of the Second National Soil Survey of China (1995) and distributed by the Institute of Soil Science in Nanjing (Shi et al., 2004). Sandy loam type soil comprises nearly 60% of the basin. It is distributed mainly in the upper reaches and mountainous areas and is decorated by sandy soil. Loam comprises nearly 40% of the area and is distributed in and around wetlands and river valleys.

Borehole soil temperature profiles were used in this research for comparison with simulation results, and were observed at in-situ stations in August 2011 (Luo et al., 2012). The locations of boreholes are shown in Fig. 1 with monitoring depths (mostly about 20 m). Boreholes were drilled in 2011 (Luo et al., 2013, 2012). Seven stations monitored ALT from 2010 to 2012 (Lin et al., 2014; Luo et al., 2014a). Some 39 in-situ ground stations monitored temperature from 2010 to 2012 (Luo et al., 2013, 2012). ALT was calculated as the deepest thaw depth from 2010 to 2012 in permafrost areas. Ground temperature at 15 m depth (GT) was used because the depth of zero amplitude ranges from 10 to 15 m depth in the Qinghai-Tibetan Plateau (Zhou et al., 2000)



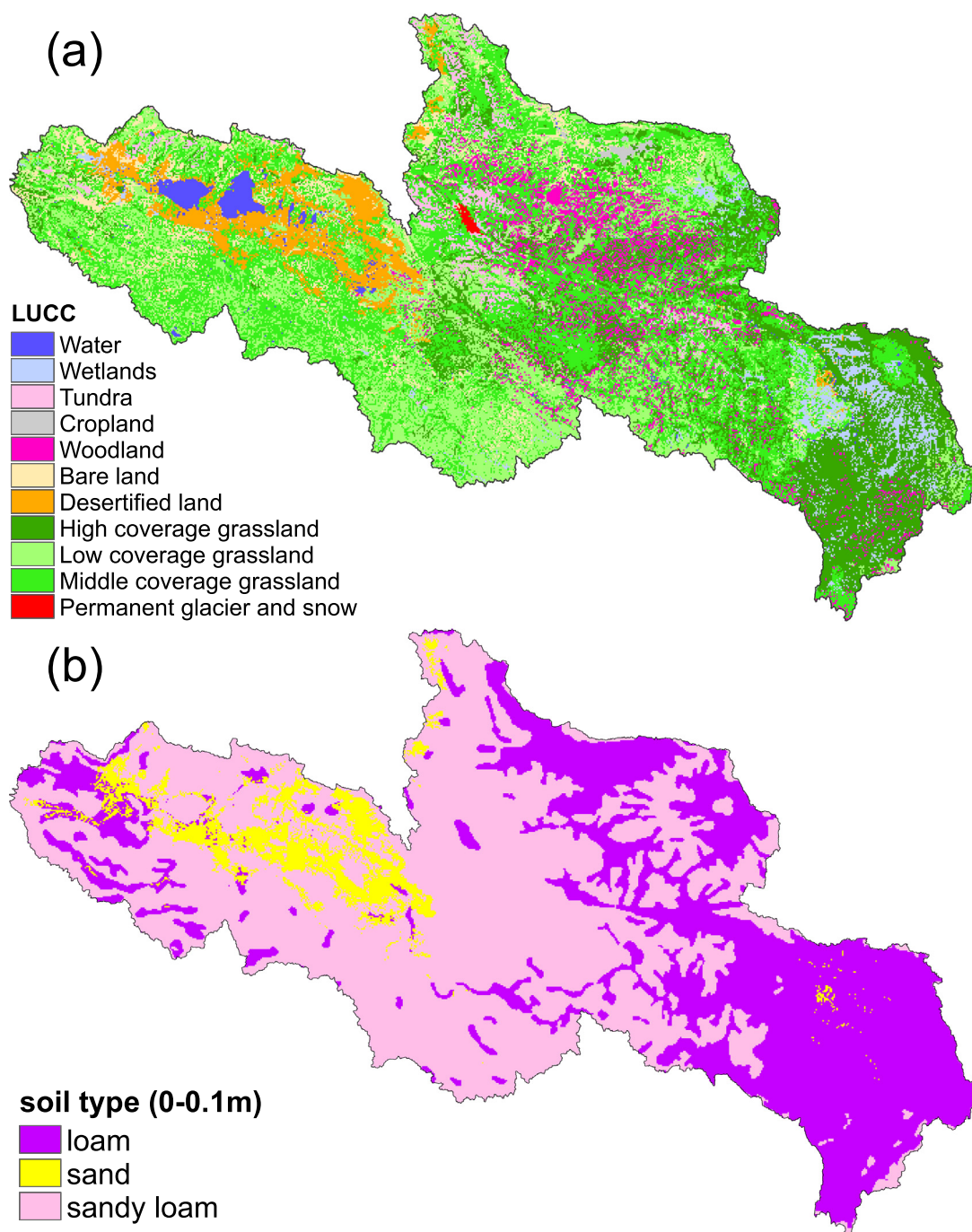


**Fig. 2.** Land use/land cover (LUCC) interpreted from remote sensing images of Landsat 1–5 Multispectral Scanner (MSS), 4–5 Thematic Mapper (TM) and 7 Enhanced Thematic Mapper Plus (ETM+) (a) and soil types from the Soil Map of China 1:1 Million scale (b) of the study area.

and to avoid the effects of seasonal temperature variation (Wu et al., 2010). GT was calculated as a mean annual value from 2010 to 2012.

Various daily meteorological forcing data were used, including precipitation, temperature, relative humidity, wind speed and sunshine duration. These data were provided by China Meteorological Data Service Center (CMDC). The data was observed in 11 China Meteorological Administration (CMA) stations (Fig. 1) in the study area. As the soil temperature was observed in 2011, this study used meteorological data from September 01, 2010 to August 31, 2012 to drive the daily model. The gridded meteorological data was spatially interpolated from weather station data. The Thiessen polygon method was used to obtain gridded precipitation. To consider the impact of topography, the daily air temperature, sunshine duration, wind speed and relative humidity

were interpolated using the elevation-dependent regression method (Schulla and Jasper, 2015, pp. 24–29).

### 3. Methods

WaSiM, which is a quasi-3D water balance simulation model (Schulla and Jasper, 2015), was used to calculate soil temperature patterns and their changes due to increased air temperatures. The model considers the underground situation, where water, ice, air and soil matrix particles mix at the same time. It has been applied widely in soil water and temperature simulations under climate change scenarios in cold regions (Gädeke et al., 2014; Jasper et al., 2004; Ollesch et al., 2006; Su et al., 2011; Warscher et al., 2013). The model uses a 1 dimensional



Richards equation to simulate the infiltration of water and considers the latent heat in phase change. The effective hydraulic conductivity is highly controlled by the relative water saturation. In turn, this is highly controlled by soil temperature. A detailed mathematical description of the model and numerical solution methods can be found in the model description (Schulla and Jasper, 2015, pp. 175–183). This research uses Model Version WaSiM-9-09-04.

The study can be subdivided into two steps: 1) evaluation of the simulation using observations and 2) evaluation of permafrost changes due to climate warming. During the first step, the meteorological forcing for the model was interpolated using weather station data from 2010 to 2012. ALT and GT were compared with observations to evaluate the model's performance. Results from the first step are regarded as the thermal state of the present-day climate scenario. During the second step, three climate warming scenarios were set, with air temperatures 1, 2 and 3 °C higher than at present (named as AT+1, AT+2, AT+3 scenarios). The climate warming scenarios were based on the magnitude of air temperature increase rather than the warming scenarios from the GCMs. The variations in soil temperature profile, GT, DPT and the permafrost maps of the present and three hypothetical scenarios were analysed to understand the 3D distribution of ground thermal states under conditions of climate change at the basin scale. A flowchart of the procedure is shown in Fig. 3.

The study area was differentiated as a  $701 \times 510$  mesh box of 1 km resolution. The vertical simulated depth for each grid cell was 29.94 m. Study requirements were that the spatial resolution should not be too fine (requiring high computing resources) nor too crude (which may not have produced satisfactory results). In this study, the resolution was determined according to the resolution of the input soil map data and the basin area, and to be suitable for subsequent hydrological simulation at the basin scale. The simulated soil depth in this study is within the reasonable range of soil data values observed in the geological survey (Cheng et al., 2005) and is consistent with previous studies (Karra et al., 2014). The valid soil depth to the bedrock in most mountain areas is far <30 m, while depths in the river valley and Zoige Plain may be deeper (Shangguan et al., 2017). However, this depth is far greater than those found in previous studies in High Asia, which usually revealed depths of around 1.2 m (Li and Sun, 2008; Wang et al., 2010; Zhang et al., 2013a). In differentiation of the heat transfer equation, the thicknesses of soil layers are not uniform in the vertical direction. Layers are thin in shallow soil and thick in deep soil because soil temperature is more sensitive to air temperature in shallow soils than in deep ones (Farbrot et al., 2013). The soil column was vertically divided into four zones, with a total of 60 layers. The topsoil zone (0–0.1 m) has only one layer, with thickness of 0.1 m. The second

zone (0.1–0.3 m) has two layers, with thickness of 0.1 m. The third zone (0.3–9.8 m) has 19 layers, with thickness of 0.5 m each. The bottom zone (9.8–29.94 m) has 38 layers, with thickness of 0.5 m each. Hydrologic and heat parameters are the same in layers of the same zone and different among different zones. Soil heat parameters, including heat capacity and thermal conductivity of dry soil, were estimated based on field surveys (Anisimov et al., 1997; Du et al., 2015; Hong et al., 2013).

The upper boundary layer for heat transfer is air temperature corrected by an  $n$ -factor. Since observations of the geothermal heat flux for the HWYR were not available at the time of data collection, the lower boundary was assumed as an upward thermal heat flux at the soil bottom with a value of  $0.03 \text{ W/m}^2$  (Wu et al., 2010). The initial soil temperature distribution was calculated based on the mean annual air temperature, mean permafrost table temperature using the TTOP method (Kudryavtsev et al., 1977), and the lower boundary condition. A 3D view of the first-guess soil temperature in this study is shown in Fig. 4. Based on initial conditions, the heat transfer equation was run for 60 years, repeating 30 cycles of runs from September 01, 2010 to August 31, 2012. This process resulted in a near-balanced 3D soil temperature pattern. The ALT does not necessarily indicate the area's largest thawing depth throughout the whole year. There may be an unfrozen layer that is overlain by a seasonally frozen/thawed layer and underlain by perennally frozen ground (Akerman et al., 1998). In this case, the thaw depth equals the sum of the thicknesses of the seasonally frozen/thawed layer and the unfrozen ground over perennally frozen ground. This summed value is the DPT, which is also the sum of ALT and talik thickness. Therefore, the DPT equals the ALT in places without talik.

## 4. Results

### 4.1. Air temperature interpolation

A spatially interpolated grid of air temperature during one day in summer is shown in Fig. 5(a). This shows great spatial variation, with high temperatures in lowland areas and low temperatures in high areas. This variation is the result of the design of the air temperature gradient and consideration of topography, including slope and aspect.

To evaluate interpolated air temperatures at a daily timescale, observations from three meteorological stations relatively close to permafrost areas, including Dari, Guoluo, and Maduo, were used for comparison. The interpolated and observed daily air temperatures are plotted for each station in Fig. 5(b–d). The figure shows that the model simulated the daily air temperatures effectively based on several measures: the

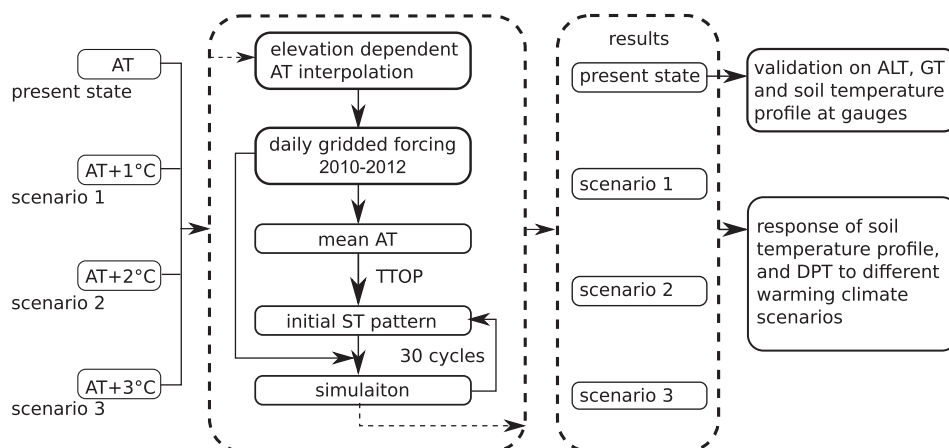


**Fig. 3.** Flowchart of methodology, AT is short for air temperature, TTOP is short for temperature at top of permafrost, ST is short for soil temperature, ALT is short for active layer thickness, GT is short for ground temperature, DPT is short for depth to permafrost table.

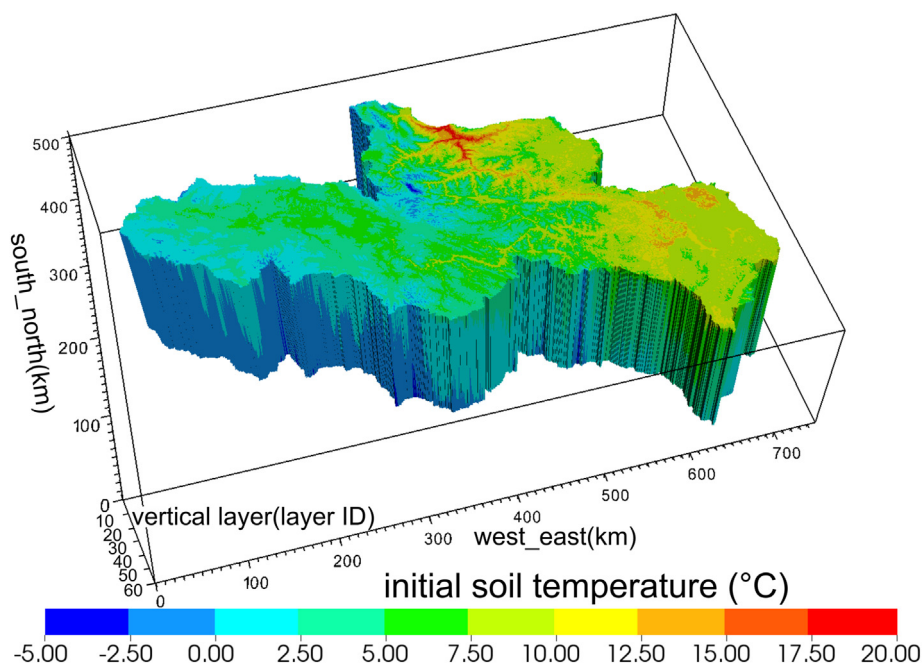


Fig. 4. 3D distribution of the initial soil temperature.

slopes of linear fitted lines,  $R$ -square values, Pearson correlation coefficients, Nash-Sutcliffe efficiencies (NSE) and root mean square errors (RMSE). This suggests that interpolated values are reasonably close to

observed ones in terms of magnitude and time. The RMSE at Dari station was 3.6 °C, which is greater than at the other two stations. This may be due to the topography at Dari, which is located in a deep river valley.

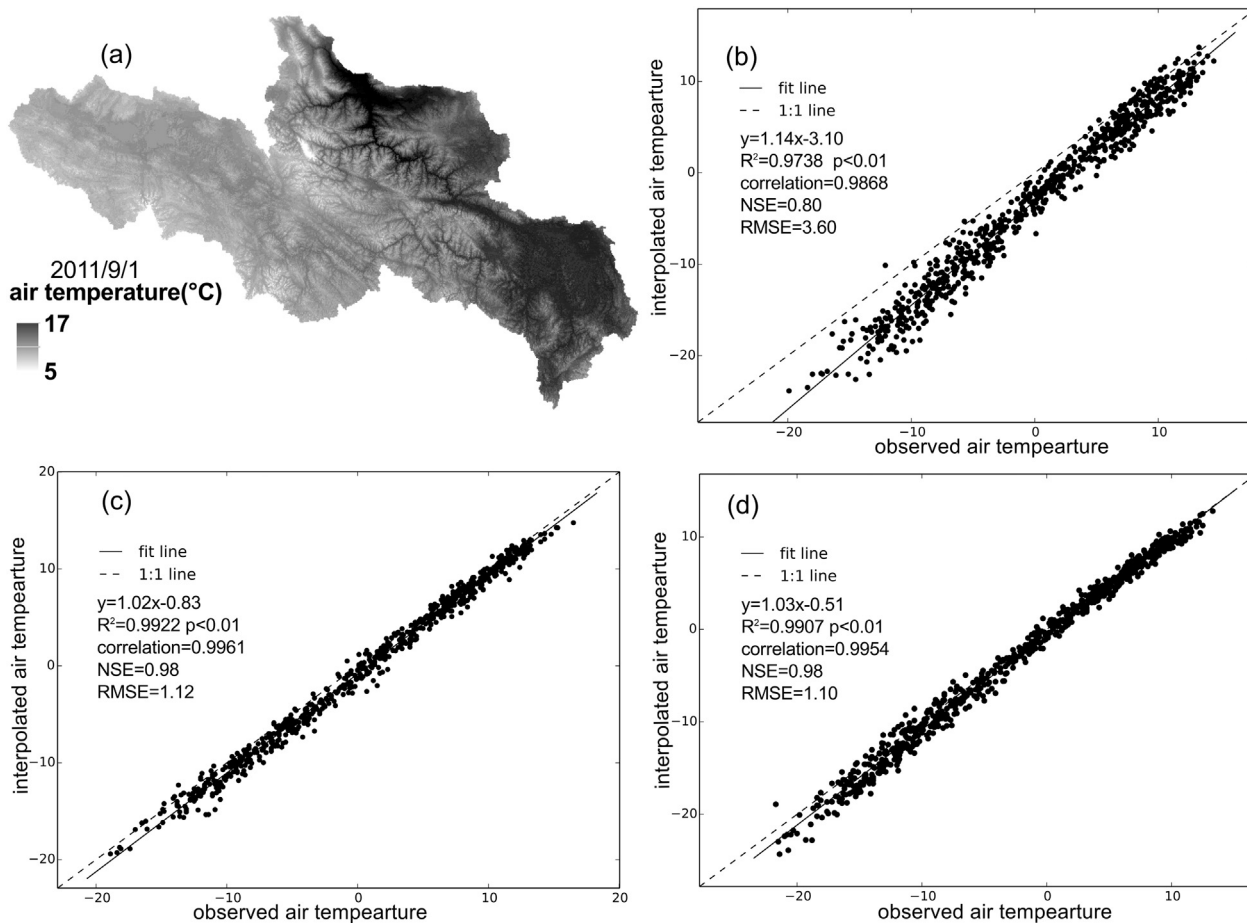


Fig. 5. Spatially interpolated air temperature at the day of September 1, 2011 (a) and compare between daily observed and interpolated air temperature from September 1, 2010 to August 31, 2012 at meteorological gauge Dari (b), Guoluo (c) and Maduo (d). The correlation is Pearson correlation coefficient.

Mountains around this station affect the air temperature through shade and changes to the local microclimate. However, our cell grid size of 1 km could smooth this effect to some extent, indicating a larger elevation for the station than is accurate. This would result in a relatively colder air in interpolation. This level of error is comparable to those of similar datasets (Luo et al., 2014b; Stahl et al., 2006).

#### 4.2. Model validation

The simulated ALT values were consistent with observations made between 2010 and 2012 at seven ALT stations and 39 in-situ ground temperature stations (Fig. 6). The Pearson correlation coefficient between simulated and observed ALT values is 0.79, demonstrating good performance of the WaSiM method in terms of ALT simulation. The linear regression  $R^2$  value was 0.62 (Fig. 6(a)), demonstrating a reasonable linear correlation between the simulated and observed ALT values. Fig. 6 (b) shows the moderate correlation between the simulated and observed ground temperatures, which had a Pearson correlation coefficient of 0.53. The linear regression here is stronger than the linear regression for ALT. This demonstrates the reasonable performance of WaSiM in the estimation of GT and ALT values at the station/point scale, with better performance in GT estimation. However, the estimated ALT values were generally higher than observed ones, while GT estimates were lower. This may be due to uncertainties in the model's

hydrological and thermal parameters. The performance of this model is generally close to the Geophysical Institute Permafrost Laboratory (GIPL) model, which is used in the source area of the Yellow River (Luo et al., 2014b), as well as Version 2 of the model (GIPL2), which is used on the Alaska North Slope (Nicolosky et al., 2017).

Estimated soil temperature profiles at three drill sites on specific days were compared with observed values (Fig. 7). The Pearson coefficients of the correlations between simulated and observed values at boreholes CLP1, K445 and MDB were 0.99, 0.91 and 0.97, respectively, with RMSEs of 1.66, 0.39 and 0.38. These high Pearson correlation coefficients indicate that the model generally captured the vertical distribution of soil temperatures at these sites in the permafrost area. However, RMSE values showed a decreasing trend from boreholes CLP1 to MDB to K445, which are geographically located from south to north and on shady to sunny slopes. Simulated positive temperatures tended to be overestimated at borehole CLP1, while negative values were consistent with observed ones. The overestimates were at locations near the ground surface at borehole CLP1, which is shady. The other two sunny boreholes had shallow soil temperatures that were consistent with the model. This indicates the model is more accurate for soil surface temperatures on sunny slopes rather than shady ones and performs well for deep soil temperatures. The model's different performance at different depths may result from its differentiation of soil layers and parameterisation of thermal conductivity.

Simulated ground temperatures at 15 m depths were compared with temperatures in the existing ground temperature map (Fig. 8 (a)). This map was made for the Yellow River source region through regression analysis based on observed soil temperatures at 15 m depths, mainly in 2013 and 2014 (Li et al., 2016a). Generally, the simulated values were consistent with the map, especially at sub-zero temperatures. Values in the area of Bayan Har Mountain were slightly lower than values on the map, especially in areas north of the two large lakes at Buqing Mountain, which had temperatures lower than  $-1^\circ\text{C}$ . In addition, the estimated values in the middle and lower reaches of the Yoigilangleb Qu river and the two large lakes were positive, while those of the map ranged from  $-0.5$  to  $0^\circ\text{C}$ . These results are due to higher air temperatures in the area in 2011 compared to 2013–2014.

#### 4.3. Results under different climate warming scenarios

##### 4.3.1. Soil temperatures in boreholes

Fig. 7 shows estimated stable soil temperature profiles under several scenarios of increasing air temperatures. It shows a general trend whereby deep soil temperatures increase wholly with increasing air temperature. In addition, other characteristics are evident. The rate of increase in soil temperature is not uniform with increasing air temperature. At CLP1, soil temperatures deeper than 5 m do not increase by  $>1^\circ\text{C}$  with an air temperature increase of  $1^\circ\text{C}$ . In contrast, higher increases of 3 and  $5^\circ\text{C}$  are estimated for the 2 and  $3^\circ\text{C}$  scenarios, respectively. The stable state of soil temperature in the  $2^\circ\text{C}$  scenario at CLP1 suggests that permafrost had already disappeared before stability was reached.

In the  $1^\circ\text{C}$  scenario at K445, the increase in soil temperature at depths shallower than 5 m was  $1^\circ\text{C}$ , which is equal to the air temperature increase. In this scenario, soils at 4–25 m depths are frozen, with temperatures just below  $0^\circ\text{C}$ . Soils  $>25$  m deep (at the bottom of the soil) were thawed. Frozen soil in this state can thaw extremely easily with a small increase in air temperature. A similar  $1^\circ\text{C}$  increase in soil temperature occurs in the 2 and  $3^\circ\text{C}$  scenarios. A nearly  $4^\circ\text{C}$  overall increase in soil temperature occurs from 1 to  $2^\circ\text{C}$  scenarios. It can be inferred that an increase in air temperature of approximately  $1.3^\circ\text{C}$  causes the disappearance of permafrost. This indicates that permafrost with a soil temperature greater than  $-0.5^\circ\text{C}$  is extremely sensitive to air warming and warms more easily than low-temperature permafrost. This phenomenon was also detected at the MDB borehole in the  $1^\circ\text{C}$  scenario, but not in borehole CLP1. This is because the soil temperature

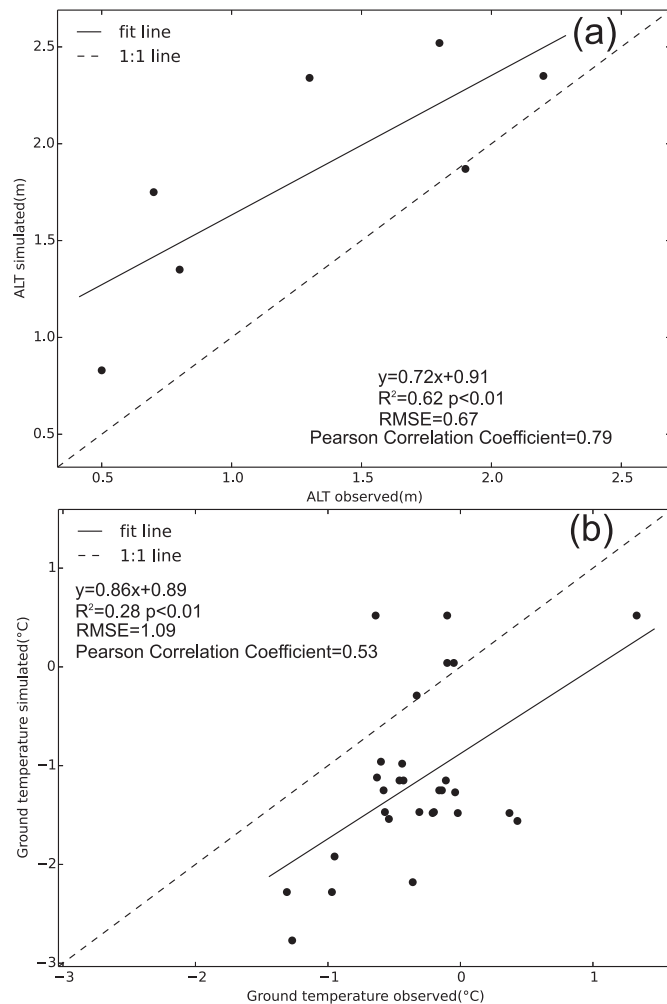


**Fig. 6.** Observed and estimated ALT (a) and ground temperature (15 m depth) (b) at different boreholes, solid lines is linear fitted of points, the dashed line is 1:1 line. The observed ALT is maximum value in several years and ground temperature is average value in several years.



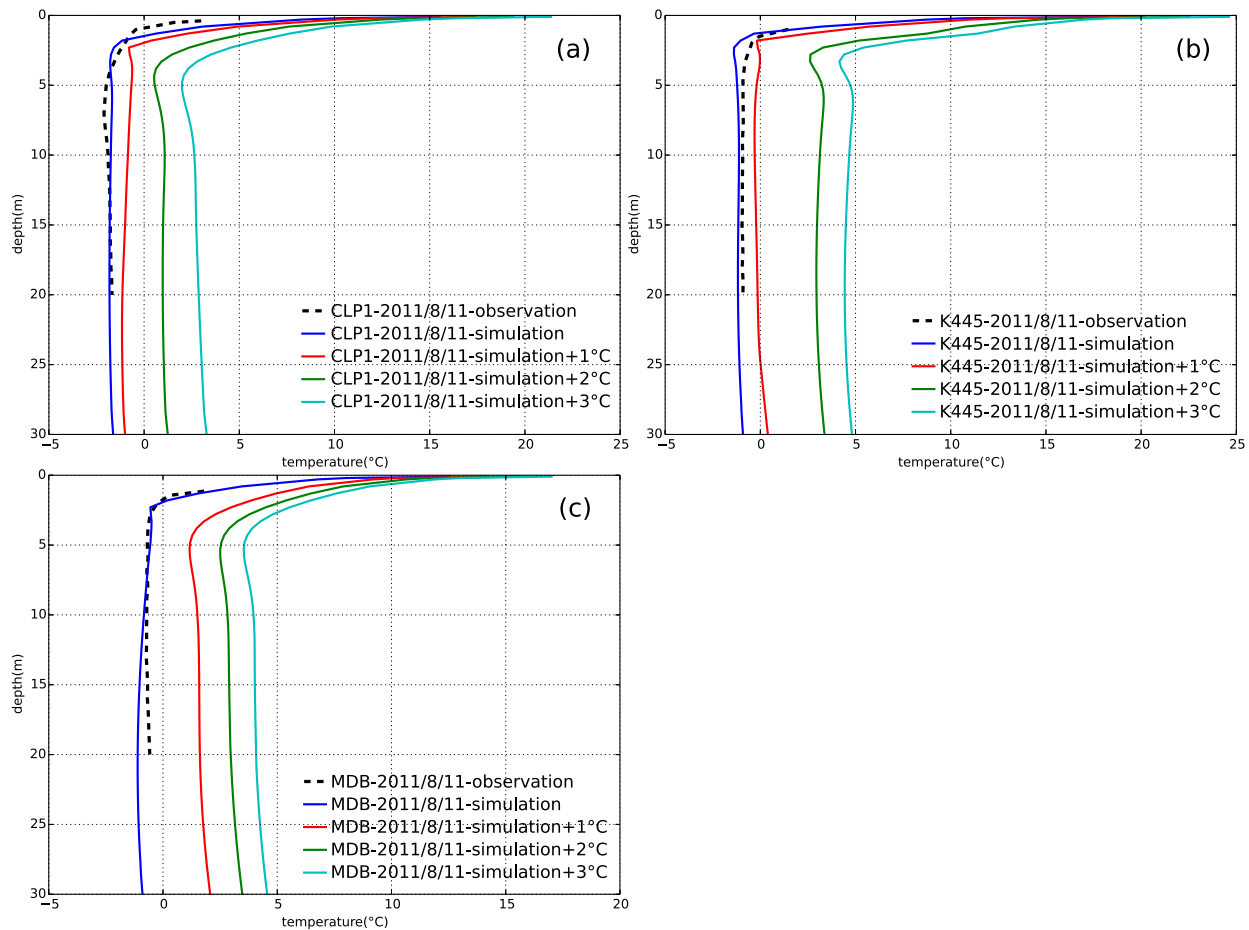


**Fig. 7.** Compare simulated (blue lines) with observed (dashed lines) soil temperature profile at day of August 11st, 2011 at borehole CLP1 (a), K445 (b) and MDB (c), changing soil temperature profiles in present state (blue lines), 1 (red lines), 2 (dark green lines) and 3 (light green lines) °C air temperature increase scenarios.

there was too low, at  $-1^{\circ}\text{C}$ . Soil temperatures at the MDB borehole increased by 3, 4.5 and  $5.5^{\circ}\text{C}$  under the 1, 2 and  $3^{\circ}\text{C}$  air warming scenarios. The last two scenarios showed homogeneous increases in soil temperature.

To understand the differences between the soil temperature increases at different boreholes under the various air temperature scenarios, correlations between soil temperature increases at the bottom of the soil column and elevation were studied (Table 1). The table shows that the rate of increase in soil temperatures with increasing air temperatures is less at higher elevations than at lower elevations. This phenomenon is clear in the 2 and  $3^{\circ}\text{C}$  scenarios and is especially strong in the  $1^{\circ}\text{C}$  scenario. The increase in soil temperature is twice that of the air at elevations below 4300 m and is 1.5 times greater above 4300 m. This suggests that soils at higher elevations are less sensitive to increases in air temperature than lower soils.

#### 4.3.2. Ground temperature at 15 m depth

The simulated 15 m-depth GT map in the present state (2011) was compared with those under three different warming scenarios (Fig. 9 (a, b, c)). A large portion of the negative ground temperatures changed to positive ones in the  $1^{\circ}\text{C}$  warmer scenario (Fig. 9(b)). The change was especially notable in mountainous areas approaching the margins of Amne Machin Mountain. Values at relatively high elevations remained negative. The proportion of basin area with sub-zero temperatures dropped from 35% (present state) to <20%, 6% and 2% in the 1, 2 and  $3^{\circ}\text{C}$  warmer scenarios. For the  $3^{\circ}\text{C}$  scenario, only tiny areas of sub-zero temperatures remained in and around mountain peaks.

The 15 m-depth ground temperatures in the basin increased from  $2^{\circ}\text{C}$  (present state) to 3.14, 4.45 and  $5.74^{\circ}\text{C}$  in the 1, 2 and  $3^{\circ}\text{C}$  warmer scenarios (Fig. 11(b)). The mean increasing rate of GT at 15 m depth in this study was  $1.25^{\circ}\text{C}$  per degree increase in air temperature. The frequency distribution of GT at 15 m depths in the basin at four scenarios is a dumbbell shape. This distribution indicates high frequency, at  $-2$ – $0$  and  $5$ – $6^{\circ}\text{C}$  in the present state, at  $-1$ – $2^{\circ}\text{C}$  and  $6$ – $7^{\circ}\text{C}$  for the  $1^{\circ}\text{C}$  scenario, at  $2$ – $4^{\circ}\text{C}$  and  $7$ – $8^{\circ}\text{C}$  for the  $2^{\circ}\text{C}$  scenario, and at  $4$ – $5^{\circ}\text{C}$  and  $8$ – $9^{\circ}\text{C}$  for the  $3^{\circ}\text{C}$  scenario. These high-frequency peaks are at the upper and lower quartile locations, which generally increase with increasing air temperature. The maximum and minimum GT values also increase with increasing air temperature. That is to say, all ground temperatures in the basin will increase without exception. This suggests there is a strong influence of air temperature on ground temperatures.

#### 4.3.3. The depth to permafrost table

DPT distributions simulated for the present state (2011) and the three warming scenarios are shown in Fig. 10(a). The present state shows that the DPT in areas near the mainstream valley is deeper than 15 m and reaches almost 30 m. This indicates that the permafrost is almost melting before forming open taliks. In the upper reaches of branched river valleys, DPT is relatively small (<2 m), especially in high mountains.

With increasing air temperature, the DPT generally increases. This finding aligns with the prediction of ALT in High Asia (Anisimov et al., 1997). The average DPT in permafrost areas increases from 5 m

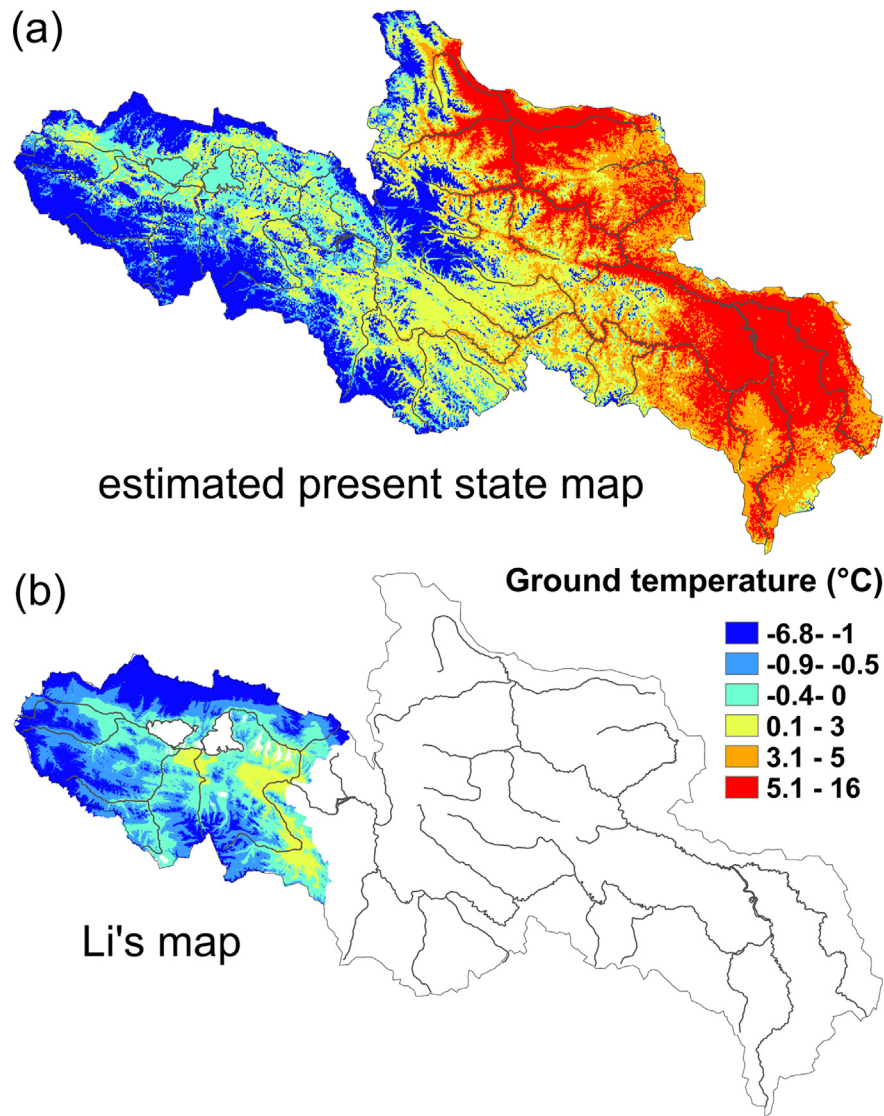


Fig. 8. Compare estimated ground temperature at 15 meter deep at present state in this study (a) to Li's map (b).

(present state) to 8 m, 10 m and 13 m under the 1, 2 and 3 °C warming scenarios, respectively (Fig. 11(a)). The mean speed of increase in DPT in the basin was 2.67 m per degree increase in air temperature. When the air temperature increases by 3 °C, there is widespread permafrost degradation, as indicated by large numbers of high DPT values. An exception is on the peak Amne Machin Mountain, where permafrost remains stable despite increasing air temperatures.

Many low DPT values in the present state exceeded 15 m in the 1 °C scenario. The conversion was particularly volatile in areas with DPT of <5 m (Fig. 10(b)). The conversion was also distinct in the region of the Bayan Har and Buqing mountains. Areas with DPTs <5 m are located

around the mountains. These areas continue to shrink in the 2 °C scenario, with just small areas remaining, including the peak Amne Machin Mountain and areas between the Kequ and Dari Rivers, the latter of which disappears in the 3 °C scenario.

Permafrost area decreased from 33% of the basin area in the present state to 20%, 7% and <3% under the 1, 2 and 3 °C scenarios, respectively. The decreases were relatively high (13%/°C) in the 2 °C scenario and low (4.6%/°C) in the 3 °C scenario. The area of 5–15 m DPT continued to increase with increases in air temperatures (Fig. 11(a)). This shows an increase in deep DPTs in permafrost areas. The frequency distribution of DPTs was mainly in the 0–5 m range in the present state, polarising with increased air temperatures into a dumbbell shape. The values were mainly in the ranges of 0–5 m and 15–25 m in the 3 °C scenario. 15–25 m values were common than 0–5 m values.

The spatial distribution of taliks in the permafrost areas in different scenarios are shown in Fig. 10(e–h). In the High Asia region, Taliks tend to develop in the river valley and low elevation areas. The area of taliks reaches the greatest value (8753 km<sup>2</sup>) in 1 °C scenario, and generally decreases in the 2 to 3 °C scenarios (Table 2). In general, area ratios of taliks to permafrost increase with climate warming. The DPT of taliks is usually deeper than 2 m and shallower than 28 m.

Table 1

Relationship between elevation of borehole and bottom temperature increase in different air temperature increase scenarios.

Name	Elevation (m)	T bottom increase (°C)		
		AT+1 °C	AT+2 °C	AT+3 °C
CLP1	4727	0.63	2.87	4.91
K445	4288	1.30	4.28	5.73
MDB	4225	2.96	4.37	5.46

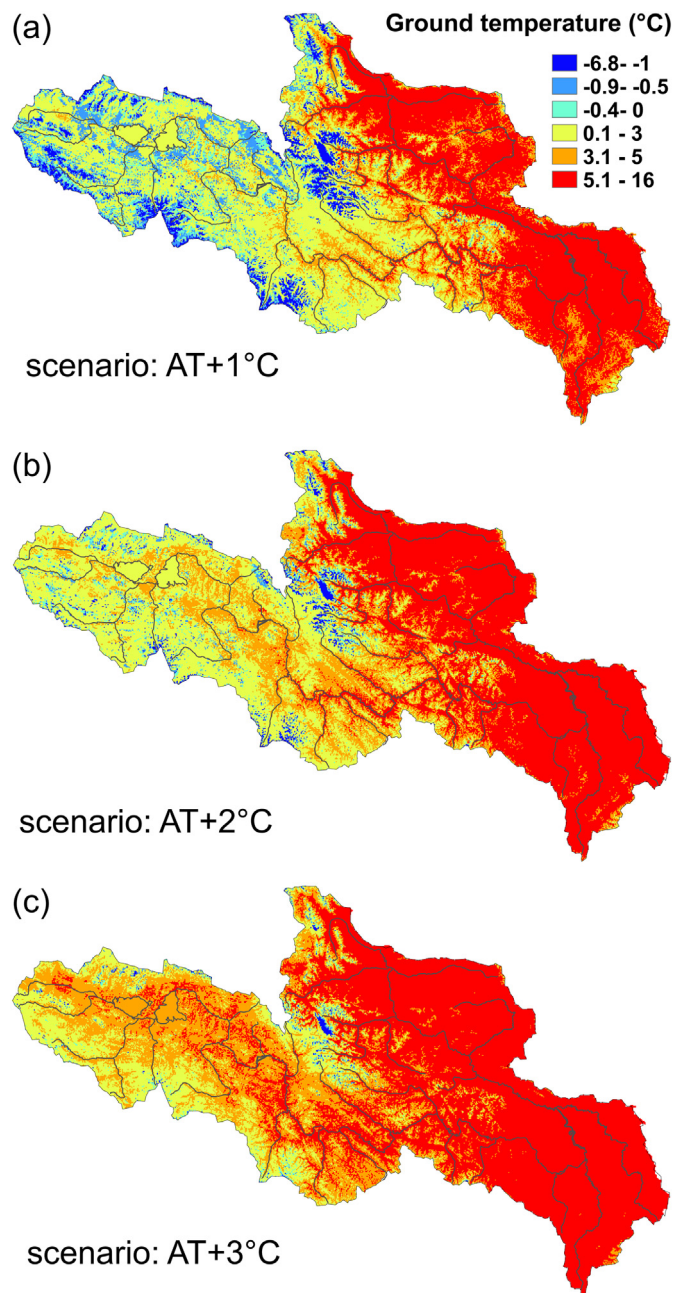


**Fig. 9.** Estimated ground temperature at 15 m depth at 1(a), 2(b) and 3 (c) °C air temperature increase scenarios.

## 5. Discussion

### 5.1. Distribution of permafrost and responses to climate warming

The focus of this study was the distribution of permafrost in the headwaters of the Yellow River. The results provide a new fine-scale map of permafrost based on a 3D mapping methodology. The new map considers local topographical factors including elevation and aspect, which greatly impact the formation of frozen ground via air temperature and radiation (Boeckli et al., 2012; Li et al., 2016a; Sheng et al., 2015; Wang et al., 2015). The permafrost map shows high variation with elevation (Table 1, Figs. 8, 9 and 10) and great differences in DPT between sunny and shady slopes (Table 3). The new map also considers taliks, which are an important part of permafrost (Walvoord and Kurylyk, 2016; Zhang et al., 2008) and have usually been omitted in previous studies (Fang et al., 2011; Qin et al., 2017; Zhao et al., 2017).

Therefore, omission of taliks could lead to overestimation of permafrost degradation, which could be one of the reasons that permafrost areas in this study were more extensive than in Qin's study (Qin et al., 2017).

In this study, permafrost with GT warmer than  $-0.5^{\circ}\text{C}$  tended to degrade more easily than colder permafrost, which is consistent with previous studies (Cheng and Wu, 2007; Wu and Zhang, 2008). The relatively larger increase of deep soil temperature than air temperature (Fig. 7 and Table 1) is due to bilateral warming characteristics from solar radiation and heat flux from the deep earth (Ling et al., 2012). Additionally, latent heat emission during thawing of deep soil amplified the warming effect when the air temperature increased by  $>1^{\circ}\text{C}$ . This usually degrades permafrost at high temperatures, or contributes to processes of transferring to seasonally frozen ground.

DPTs were larger on sunny slopes than shady ones (Table 3). This highlights the impact of the interaction between solar radiation and terrain. Differences of DPT between sunny and shady slopes tended to be greater with larger air temperature increases. The different amounts of energy received by topsoil on sunny and shady slopes cause differences in surface temperature. In turn, this creates different upper boundaries for heat transfer in the soil column. This results in larger DPT and more rapid degradation of permafrost on sunny slopes than shady ones (Cheng, 2004; Gao et al., 2016; Lewkowicz and Ednie, 2004).

The equilibrium results of permafrost in this study reveal the condition of permafrost and its responses to climate warming. Climate warming is the most critical effect of climate change. A 2018 special report by the Intergovernmental Panel on Climate Change (IPCC) notes that air temperature has increased  $1.5^{\circ}\text{C}$  from pre-industrial levels. This warming will continue in the future, according to CMIP5 projections. Thus, assumed increases from current air temperatures imply future climate warming. If it is assumed that air temperature will increase by  $0.25^{\circ}\text{C}$  per decade, the  $1^{\circ}\text{C}$  scenario in this study could represent climate conditions in four decades' time. The result of this scenario would affect future permafrost levels. Permafrost, which is the equilibrium state of frozen ground, is the average state of frozen ground across several decades. In transient modelling, permafrost is usually the result of the climate of the previous several decades. Thus, it is acceptable that results derived under conditions of assumed increasing air temperature repeated over several decades indicate the equilibrium state of frozen ground under conditions of future climate warming.

Several previous studies have predicted permafrost responses to climate warming (Anisimov et al., 1997; Cheng, 1998; Nicolsky et al., 2017; Zhang et al., 2008). The permafrost degradation rate estimated for the HWYR in this study was 36% per degree increase in air temperature. Studies in the QTP have estimated rates of  $6\%/^{\circ}\text{C}$  (Nan et al., 2005),  $17\%/^{\circ}\text{C}$  (Cheng, 1984) and  $22.7\%/^{\circ}\text{C}$  (Wang et al., 2019). In Canada, the rate is  $4\%/^{\circ}\text{C}$  (Zhang et al., 2008). The degradation rate can be generally ranked as HWYR > QTP > Canada. Therefore, despite the uncertainties in individual models, methods and data, it can be inferred that permafrost in the HWYR is generally more sensitive than that in High Asia overall, which, in turn, is more sensitive than permafrost in Canada.

### 5.2. Comparison with previous studies

Numerous permafrost maps have been produced using field survey or conceptual empirical methods (Ran et al., 2012). Three well-known previous permafrost maps are shown in Figs. 12 and 1. These three maps used similar data sources (remote sensing images) but at different times. The 1988 map (Fig. 12(a)) is based on field surveys, observations, long-term site monitoring, maps, aerial photographs and terrain analysis (Shi and Mi, 1988). The 1996 map (Li and Cheng, 1996; Fig. 12(b)) is comprehensively interpreted based on permafrost surveys, with reference to the 1988 map, field data, relevant literature and many other relevant maps (Institute of Geographic Science, Chinese, 1990, 1985; Li and Li, 1991; LIGG/CAS, 1995). The 2006 map (Fig. 1) was



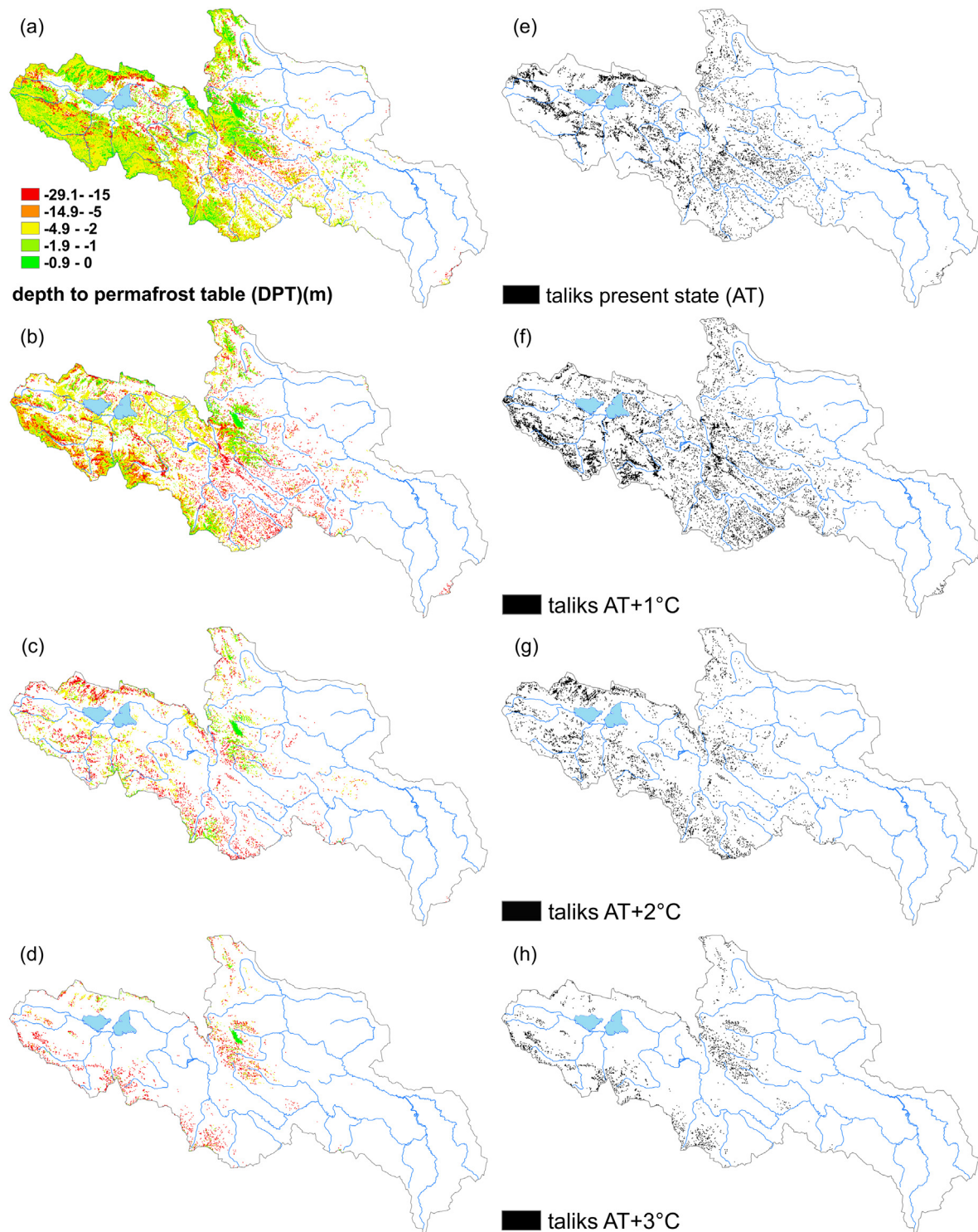


**Fig. 10.** Simulated DPT at present state (a), 1 (b), 2 (c), and 3 (d) °C air temperature increase scenarios. The negative values mean underground direction. Namely, the greater the absolute negative value is, the deeper the DPT is and vice versa, (e, f, g, h) are the spatial distribution of taliks in different scenarios.

drawn using new data based on the relationship between MAGT and elevation (Wang, 2006). In this map, permafrost is classified as latitudinal and altitudinal permafrost (Ran et al., 2012). These three maps have similarities: they show general increases in permafrost continuity from southeast to northwest, and that permafrost is widely distributed in mountainous areas rather than river valleys. However, areas of permafrost differ in the upper Maduo watershed and around Guoluo station. The permafrost upstream of Maduo, covering two lakes, is continuous in the 1988 and 1996 maps, but thaws at two lakes in the

2006 map. A large permafrost zone around Guoluo meteorological station in the 1988 and 1996 maps is greatly degraded in the 2006 map. The differences among these three maps may be due to permafrost degradation, advancements in mapping technology, or different data availability. These factors, and the warming climate, make the 2006 map the closest to the present map (2011; Fig. 12(c)). Additionally, the area of permafrost is 62,249 km<sup>2</sup> in the 1988 map, 67,296 km<sup>2</sup> in the 1996 map, 41,985 km<sup>2</sup> in the 2006 map and 40,365 km<sup>2</sup> in 2011, covering 51%, 55%, 34% and 33% of the basin area, respectively.

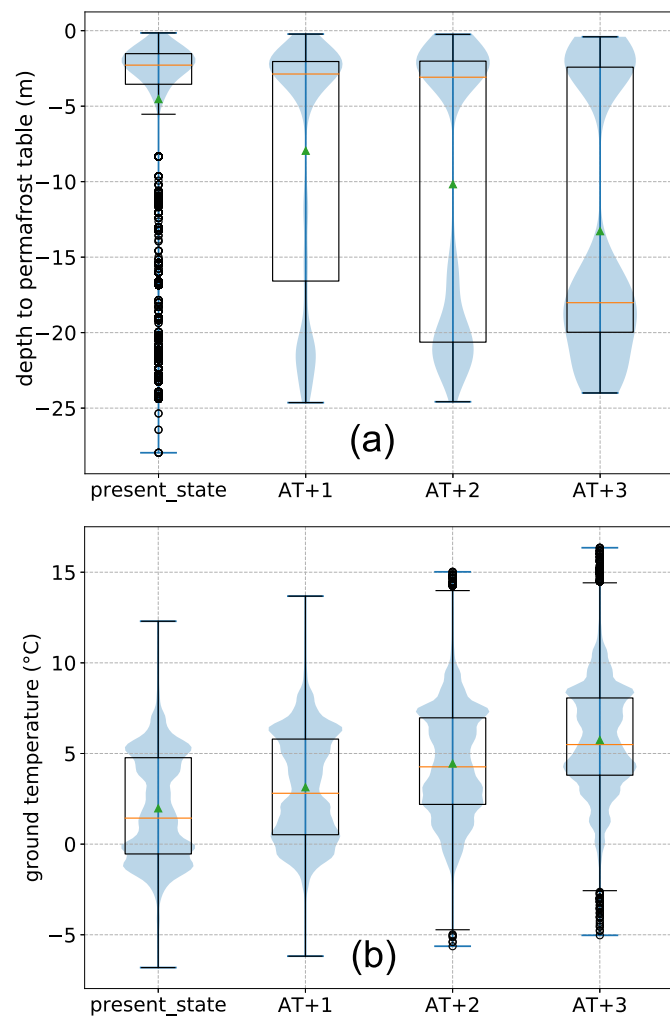


**Fig. 11.** Statistics (boxplot) and frequency distribution (voilin plot in light blue color) of depth to permafrost table DPT (a) and ground temperature (GT) at 15 m deep (b) in the HWYR for different air temperature (AT) increase scenarios. AT+1, AT+2 and AT+3 means air temperature increased by 1, 2 and 3 °C. The negative values in (a) represent underground. The small green triangles show mean values.

The permafrost map used in this study generally accords with the 2006 map. Both depict similar extents of permafrost degradation in mountainous areas to the south of the two lakes, around Guoluo, in the northern valleys, around Guoluo meteorological station, and on Amne Machin Mountain, which is located in the north-central region of the HWYR basin. Compared to the 2006 map, the present study's map shows degraded permafrost in the river valley of the upper Gyaring Lake, where permafrost exists in the 2006 map. It also shows a greater permafrost distribution on the southern slope of the river valley from the Maduo to Jiuzhi meteorological stations. These differences show a more reasonable simulation result than the 2006 map. The annual

**Table 2**  
Talík area, its ratio to permafrost areas and other statistics values in different scenarios.

Scenarios	Talik area (km <sup>2</sup> )	Ratio	max-DPT (m)	min-DPT (m)	mean-DPT (m)
AT	6302	16%	−3.93	−27.96	−17.41
AT+1 °C	8753	36%	−1.90	−24.64	−18.44
AT+2 °C	4269	49%	−2.57	−24.58	−18.76
AT+3 °C	1995	64%	−5.50	−24.00	−19.51

**Table 3**

Mean DPT and differences between sunny and shady slopes in permafrost area in different scenarios. The sunny slopes are southwards and shady is northwards.

	AT	AT+1 °C	AT+2 °C	AT+3 °C
Shady (m)	−4.52	−7.02	−8.73	−12.59
Sunny (m)	−4.54	−8.84	−11.42	−14.16
Differences (m)	0.02	1.81	2.7	1.57

average air temperature in 2011 was 1 °C higher than in 2006. In addition, the simulation in this study considered fine land surface variations, including land use, soil type, elevation, slope and aspect. Aspect particularly impacts the amount of energy that topsoil receives, as permafrost degrades more rapidly on sunny slopes than shaded ones, which is consistent with previous findings (Cheng, 2004; Gao et al., 2016; Lewkowicz and Ednie, 2004). Moreover, the simulated map is based on a fine, physically-based, distributed, quasi-3D model. In contrast,

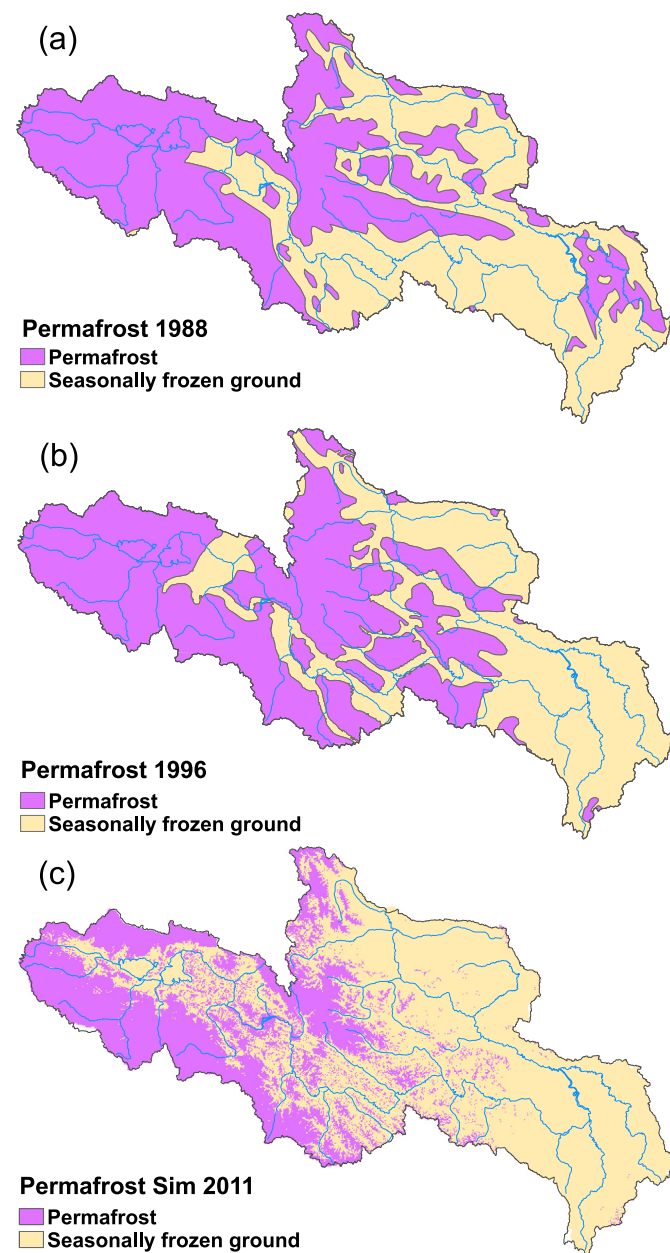


**Fig. 12.** Compare between estimated permafrost map (c) and existing ones in year 1988 (a) and 1996 (b).

the 2006 map was conceptual, empirical and large-scale. Additionally, the permafrost area in this study is nearly double the area identified by Qin et al. (2017). These differences may be due to differences in modelling and permafrost characterisation methods. Qin characterised a grid as permafrost when the frozen ground depth was greater than zero year-round. Based on this view, this research considered taliks, where an unfrozen layer is overlain by a seasonally frozen/thawed layer and underlain by perennally frozen ground. Taliks have been ignored in most previous research on permafrost, making this study's estimates of permafrost areas larger than what is suggested by Qin's results. These advantages give the simulated results high heterogeneity, a more reasonable distribution of permafrost, and high congruence to the natural world. The simulation is relevant to current climate science research and provides more detailed information for application to the management of environments and infrastructure in cold regions.

The present permafrost areas simulated in this study are consistent with frozen soil in the 2000s that was estimated using a regression equation (Fang et al., 2011). However, the simulated value is larger than the 17% simulated in Qin's study (Qin et al., 2017). The simulated value is smaller than the value simulated for 2006 in the source region of the Yellow River using the GIPL model (Luo et al., 2014b). It is also smaller than the value simulated for 1991–2010 using the TTOP method (Wang et al., 2018). These differences may be due to different mapping techniques, data availability, and differences in models and methods. Comparing permafrost maps of the QTP using five models including ELEV, MAGT, ROSNUM, TTOP and K-MODEL, the permafrost distribution estimated by the present study is closer to that of MAGT than the other four models (Zhao et al., 2017).

According to the gradient of increasing air temperature (0.25 °C per decade) estimated from RCP4.5 results of GCMs, the Fifth Assessment Report (AR5) of the IPCC (Stocker et al., 2013), the permafrost in the 1 °C scenario may represent its state in the year 2051. In the same way, the permafrost in the 2 and 3 °C scenarios could represent conditions in the years 2091 and 2131, respectively. Therefore, differences in soil temperature profile, spatial DPT and GT in the present and 1, 2, and 3 °C warming scenarios represent the thermal responses of soils to the climate warming predicted to occur between 2011 and 2131. Therefore, permafrost will be degraded before 2051 at the MDB and CLP1 stations, while K445 will be degraded before 2091. Areas of permafrost in the region, which currently comprise 33% of the basin area, will decrease to 20%, 7% and 3% in 2051, 2091 and 2131, respectively. This will occur at speeds of 0.325%, 0.325% and 0.1% per year, respectively. This rate of decrease has been reported to be 1.1% per year from 1981 to 2015 (Qin et al., 2017), which is about three times greater than we predicted for 2011–2091 and 10 times greater than our prediction for 2091–2131. These differences may be due to the severity of climate warming in the late 20th century compared to future climate warming, as predicted by GCMs with normal emissions scenarios. The mean rate of increasing air temperature in Qin's research was 0.66 °C per decade, which is twice the rate estimated in the present study. This rate may result in relatively warmer permafrost and smaller permafrost area than this study.

The magnitudes of increasing GT in this study are smaller than the mean annual 2 m-depth ground temperatures estimated across the Alaska North Slope (Nicolosky et al., 2017). They are also smaller than that of high temperature permafrost and greater than that of low temperature permafrost in High Asia (Wu et al., 2005) based on the air temperature gradient estimated in RCP4.5 of GCMs in the IPCC AR5. This is because shallow frozen soil is more sensitive to air temperature than deep soil. The mean rate of increasing GT at 15 m depth in this study is 0.55 °C higher than that in permafrost areas in Canada (Zhang et al., 2008).

The magnitude of increase of DPT is about 3 m greater than the increase across the Alaska North Slope based on the temperature gradient from RCP4.5 of GCMs (Nicolosky et al., 2017). This may be due to the calculation of DPT considering the thickness of talik. The mean speed

of increase in DPT in this study is more than four times greater than the mean value (0.59 m/°C) in Canada based on six GCM models (Zhang et al., 2008). This suggests that permafrost in the HWYR is more sensitive to changes in air temperature than permafrost across the Alaska North Slope (Cheng, 1998). In terms of permafrost areas in the present state, 39% will be lost in the 1 °C scenarios. This figure amounts to more than twice the area of the Qinghai-Tibetan Plateau (QTP; Cheng, 1984). In the 3 °C scenario, 91% of permafrost will be lost, which is 33% more than the area of the QTP, based on predictions using altitude and empirical models (Cheng, 1984).

### 5.3. Uncertainties and limitations

The differences between the estimated and observed soil temperatures may be due to sub-grid heterogeneity, as well as uncertainty in thermal parameters, land use and soil types. Sub-grid heterogeneity is mainly caused by variation in local factors, including elevation, slope, aspect, land use/land cover, soil types and snow depth. One previous study showed that borehole observations may have quite different soil temperature profiles to others 28 m away (Gruber et al., 2004), with a bias from 0.5 to 1.5 °C all along the 17 m soil depth. The differences between simulated and observed soil temperatures in this study were <0.8 °C, which is consistent with bias in Gruber's study. This shows the good performance of this study's model in simulating soil temperatures. Additionally, the cell size used in the simulations was 1 km, which is 30 times greater than the distance between the two observation boreholes in Gruber's study. We used large cell sizes but did not produce major errors. Therefore, the performance of the model in simulating soil temperature is acceptable.

The soil temperature simulation considered water conduction and its influence on energy transfer. Heat advection needs to be considered at resolutions finer than 1 km (Jafarov et al., 2012). We did not consider heat advection in this study because there were no suitable soil moisture or groundwater observations available for validation. Thus, more field research should be carried out in the future for consideration of seasonal and inter-annual variation in hydrological processes. These include evapotranspiration, surface routing of water between grids, flooding in rivers and interactions between surface water and groundwater, which might impact the energy exchange between air and deep soils. Hence, there is an increasing need to construct historical 3D permafrost distribution maps for the HWYR, with more focus on detailed analyses of the relationships between surface water and ground thermal states based on long-term simulation. In addition, simulation at large depths will be carried out in the future to investigate thermal dynamics in deep soils.

## 6. Conclusions

In this study, a fine-scale map of permafrost distribution and degradation according to assumed increases in air temperature was constructed for the headwaters of the Yellow River. The performance of the air temperature interpolation method was evaluated. The simulation was validated using observed soil temperature, active layer thickness and ground temperature data from boreholes. The spatial distribution of depth-to-permafrost and 15 m-depth ground temperature was analysed, and the characteristics of permafrost degradation under a warming climate were discussed.

Considering taliks and local factors including elevation and aspect, the WaSim model successfully simulated the 3D distribution of permafrost and achieved a fine-scale map at the basin scale. Permafrost will experience clear degradation in a warming climate. From the present state to the three warming scenarios (air temperature increases of 1, 2 and 3 °C), the area of permafrost in the basin will decrease from 33% to 20%, 7% and 3%. This will occur at a mean degradation rate of 36%/°C. The average ground temperature at 15 m depth will increase from 2 °C to 3.14 °C, 4.45 °C and 5.74 °C at a mean rate of 1.25 °C/°C.



Mean DPT in permafrost zones will increase from 5 m to 8 m, 10 m and 13 m, at a mean rate of 2.67 m/°C. The distribution and variation in soil temperature profile, GT and DPT indicate that permafrost is more sensitive at low elevations and on sunny slopes.

Further simulations and analyses based on coupled heat and hydrology processes in this basin are required to improve simulations of soil temperature and DPT. More observations of soil temperature and moisture are necessary to understand the interactions between changing hydrology processes and permafrost under conditions of climate warming. The simulated permafrost map in this study can be used in the study of permafrost distribution, the design of infrastructural projects in cold regions, road maintenance in the basin, and to help manage ecosystem elements such as sand dunes, swamps, wetlands and tundra.

## Acknowledgements

This work was supported by the National Natural Science Foundation of China (Grant No. 51539003, 41630856, 41471016); Thanks for the data support from “National Earth System Science Data Sharing Infrastructure, National Science & Technology Infrastructure of China. (<http://www.geodata.cn>)”. Thanks are also given to Jörg Schulla, the model developer, for many of his help on model settings and parameter adjustments. We are very grateful to anonymous reviewers whose comments helped improve the paper considerably.

## References

- Akerman, H., Barry, R., Brown, J., Buk, E., Cheng, G., Corte, A., Dramis, F., Ferrians Jr., O., Gregersen, O., Hall, K., Harris, S., Heginbottom, J., Karte, J., King, L., Konishchev, V., Kozarski, S., Ladanyi, B., Leibman, M., Lautridou, J., Marks, L., Ottone, C., Palacios, D., Petursson, H., Pissart, A., Qiu, G., Pelelewska-Pekalowa, J., Romanovskii, N., Salvigsen, O., Seppala, M., Shur, Y., Tarnocai, C., Trombotto, D., Ugolini, F., van Vliet-Lanoë, B., Zhao, X., Zhou, Y., 1998. Multi-language Glossary of Permafrost and Related Ground-ice Terms. International Permafrost Association, The Arctic Institute of North America The University of Calgary, Calgary, Alberta, Canada.
- Anisimov, O.A., Shiklomanov, N.I., Nelson, F.E., 1997. Global warming and active-layer thickness: results from transient general circulation models. *Glob. Planet. Chang.* 15, 61–77. [https://doi.org/10.1016/S0921-8181\(97\)00009-X](https://doi.org/10.1016/S0921-8181(97)00009-X).
- Boeckli, L., Brenning, A., Gruber, S., Noetzi, J., 2012. A statistical approach to modelling permafrost distribution in the European Alps or similar mountain ranges. *Cryosphere* 6, 125–140. <https://doi.org/10.5194/tc-6-125-2012>.
- Briggs, M.A., Walvoord, M.A., McKenzie, J.M., Voss, C.I., Day-Lewis, F.D., Lane, J.W., 2014. New permafrost is forming around shrinking Arctic lakes, but will it last? *Geophys. Res. Lett.* 41, 2014GL059251. <https://doi.org/10.1002/2014GL059251>.
- Bring, A., Fedorova, I., Dibike, Y., Hinzman, L., Mård, J., Mernild, S.H., Prowse, T., Semenova, O., Stuefer, S.L., Woo, M.-K., 2016. Arctic terrestrial hydrology: a synthesis of processes, regional effects, and research challenges. *J. Geophys. Res. Biogeosci.* 121, 2015JG003131. <https://doi.org/10.1002/2015JG003131>.
- Cheng, G., 1984. Problems of zonation of high-altitude permafrost. *Acta Geograph. Sin.* 39, 185–193.
- Cheng, G., 1998. Glaciology and geocryology of China in the past 40 years: progress and prospect. *J. Glaciol. Geocryol.* 20, 213–226.
- Cheng, G., 2004. Influences of local factors on permafrost occurrence and their implications for Qinghai-Xizang Railway design. *Sci. China Ser. D Earth Sci.* 47, 704–709. <https://doi.org/10.1007/BF02893300>.
- Cheng, G., Wu, T., 2007. Responses of permafrost to climate change and their environmental significance, Qinghai-Tibet Plateau. *J. Geophys. Res. Earth Surf.* 112, F02S03. <https://doi.org/10.1029/2006JF000631>.
- Cheng, J., Jiang, M., Zan, L., Liu, X., Xu, X., Lu, P., Zhang, X., Tian, M., 2005. Progress in research on the quaternary geology in the source area of the Yellow River. *Geoscience* 19, 239–246.
- Connon, R.F., Quinton, W.L., Craig, J.R., Hayashi, M., 2014. Changing hydrologic connectivity due to permafrost thaw in the lower Liard River valley, NWT, Canada. *Hydrol. Process.* 28, 4163–4178. <https://doi.org/10.1002/hyp.10206>.
- Cuo, L., Zhang, Y., Bohn, T.J., Zhao, L., Li, J., Liu, Q., Zhou, B., 2015. Frozen soil degradation and its effects on surface hydrology in the northern Tibetan Plateau. *J. Geophys. Res.-Atmos.* 120, 8276–8298. <https://doi.org/10.1002/2015JD023193>.
- Du, Y., Li, R., Wu, T., Xie, C., Xiao, Y., Hu, G., Wang, T., 2015. Study of soil thermal conductivity: research status and advances. *J. Glaciol. Geocryol.* <https://doi.org/10.7522/j.issn.1000-0240.2015.0119>.
- Fang, Y., Qin, D., Ding, Y., 2011. Frozen soil change and adaptation of animal husbandry: a case of the source regions of Yangtze and Yellow Rivers. *Environ. Sci. Pol.* 14, 555–568. <https://doi.org/10.1016/j.envsci.2011.03.012>.
- Farbrøt, H., Isaksen, K., Etzelmüller, B., Gishnas, K., 2013. Ground thermal regime and permafrost distribution under a changing climate in Northern Norway. *Permafr. Periglac. Process.* 24, 20–38. <https://doi.org/10.1002/ppp.1763>.
- Feng, S., Tang, M., 1998. A new evidence that the Qinghai-Tibet Plateau is the start-up zone of climate change in China. *Chin. Sci. Bull.* 43, 633–636.
- Gädeke, A., Hölzel, H., Koch, H., Pohle, I., Grünwald, U., 2014. Analysis of uncertainties in the hydrological response of a model-based climate change impact assessment in a subcatchment of the Spree River, Germany. *Hydrol. Process.* 28, 3978–3998. <https://doi.org/10.1002/hyp.9933>.
- Gao, T., Zhang, T., Wan, X., Kang, S., Sillanpää, M., Zheng, Y., Cao, L., 2016. Influence of microtopography on active layer thaw depths in Qilian Mountain, northeastern Tibetan Plateau. *Environ. Earth Sci.* 75, 1–12. <https://doi.org/10.1007/s12665-015-5196-7>.
- Gruber, S., King, L., Kohl, T., Herz, T., Haeberli, W., Hoelzle, M., 2004. Interpretation of geothermal profiles perturbed by topography: the alpine permafrost boreholes at Stockhorn Plateau, Switzerland. *Permafr. Periglac. Process.* 15, 349–357. <https://doi.org/10.1002/ppp.503>.
- Haeberli, W., Käbb, A., Hoelzle, M., Bösch, H., Funk, M., Mühll, D.V., Keller, F., 1999. *Eissschwind und Naturkatastrophen im Hochgebirge*. vdf, Hochschulverlag AG an der ETH.
- Harris, C., Haeberli, W., Vonder Mühll, D., King, L., 2001. Permafrost monitoring in the high mountains of Europe: the PACE project in its global context. *Permafr. Periglac. Process.* 12, 3–11. <https://doi.org/10.1002/ppp.377>.
- Heginbottom, J.A., 2002. Permafrost mapping: a review. *Prog. Phys. Geogr.* 26, 623–642. <https://doi.org/10.1191/0309133302pp355ra>.
- Heginbottom, J.A., Radburn, L.K., Narraway, J.D., 1992. *Permafrost and ground ice conditions of northwestern Canada*. p. 1691A.
- Hong, T., Liang, S., Sun, Y., Zhao, Z., Hao, Y., Wang, X., Wan, L., 2013. Analyzing the factors that impact on the heat conductivity coefficient and applying them to simulate the depth of permafrost active layer in the headwaters of the Yellow River. *J. Glaciol. Geocryol.* 97, 1079–1084. <https://doi.org/10.7522/j.issn.1000-0240.2013.0093>.
- Huang, R., Zhou, D., 2012. The impact of climate change on the runoff of the Yellow River and ecosystem and frozen soil in its source area. *Chin. J. Nat.* 34, 1–9. <https://doi.org/10.3969/j.issn.0253-9608.2012.01.001>.
- Institute of Geographic Science, Chinese, 1985. *Geomorphic Map of Middle Part of Qilian Mountains (1:1000000)*.
- Institute of Geographic Science, Chinese, 1990. *Landscape Map of the Qinghai-Tibetan Plateau (1: 3000000)*.
- Jafarov, E.E., Marchenko, S.S., Romanovsky, V.E., 2012. Numerical modeling of permafrost dynamics in Alaska using a high spatial resolution dataset. *Cryosphere* 6, 613–624. <https://doi.org/10.5194/tc-6-613-2012>.
- Jansson, P.E., Karlberg, L., 2001. *Coupled Heat and Mass Transfer Model for Soil-plant-atmosphere Systems*. Division of Land & Water Resources, Depart. of Civil and Environ. Engineering, Royal Institute of Technology, Stockholm.
- Jasper, K., Calanca, P., Gyalistras, D., Fuhrer, J., 2004. Differential impacts of climate change on the hydrology of two alpine river basins. *Clim. Res.* 26, 113–129. <https://doi.org/10.3354/cr026113>.
- Jiang, Y., Zhuang, Q., O'Donnell, J.A., 2012. Modeling thermal dynamics of active layer soils and near-surface permafrost using a fully coupled water and heat transport model. *J. Geophys. Res.-Atmos.* 117, D11110. <https://doi.org/10.1029/2012JD017512>.
- Jin, H., Yu, S., Guo, D., Lv, L., Li, Y., 2006. Degradation of permafrost in the Da and Xiao Hinggan Mountains, Northeast China, and preliminary assessment of its trend. *J. Glaciol. Geocryol.* 28, 467–476.
- Jin, H.J., Chang, X.L., Wang, S.L., 2007. Evolution of permafrost on the Qinghai-Xizang (Tibet) Plateau since the end of the late Pleistocene. *J. Geophys. Res. Earth Surf.* 112, F02S09. <https://doi.org/10.1029/2006JF000521>.
- Karra, S., Painter, S.L., Lichtner, P.C., 2014. Three-phase numerical model for subsurface hydrology in permafrost-affected regions (PFLOTTRAN-ICE v1.0). *Cryosphere* 8, 1935–1950. <https://doi.org/10.5194/tc-8-1935-2014>.
- Koven, C.D., Riley, W.J., Stern, A., 2012. Analysis of permafrost thermal dynamics and response to climate change in the CMIP5 earth system models. *J. Clim.* 26, 1877–1900. <https://doi.org/10.1175/JCLI-D-12-00228.1>.
- Kudryavtsev, V., Garagula, L., Kondratyeva, V., 1974. *Foundation of Geocryology*. Moscow State University Press, Moscow, Russia.
- Kudryavtsev, V.A., Garagulya, L.S., Yeva, K.A.K., Melamed, V.G., Kudryavtsev, V.A., Garagulya, L.S., Yeva, K.A.K., Melamed, V.G., 1977. *Fundamentals of Frost Forecasting in Geological Engineering Investigations (Osnovy Merzlotnogo Prognoza pri Inzhenerno-Geologicheskikh Issledovaniyakh)* (DTIC Document).
- Kurylyk, B.L., Hayashi, M., Quinton, W.L., McKenzie, J.M., Voss, C.I., 2016. Influence of vertical and lateral heat transfer on permafrost thaw, peatland landscape transition, and groundwater flow. *Water Resour. Res.* 52, 1286–1305. <https://doi.org/10.1002/2015WR018057>.
- Lemke, P., Ren, J., Alley, R.B., Allison, I., Carrasco, J., Flato, G., Fujii, Y., Kaser, G., Mote, P., Thomas, R.H., Zhang, T., 2007. *Observations: Changes in Snow, Ice and Frozen Ground*.
- Lewkowicz, A.G., Ednie, M., 2004. Probability mapping of mountain permafrost using the BTS method, Wolf Creek, Yukon Territory, Canada. *Permafr. Periglac. Process.* 15, 67–80. <https://doi.org/10.1002/ppp.480>.
- Li, S., Cheng, G., 1996. *Map of Frozen Ground on Qinghai-Xizang Plateau*.
- Li, B., Li, J., 1991. *Quaternary Glacial Distribution on the Qinghai-Tibetan Plateau (1: 3000000)*.
- Li, Q., Sun, S., 2008. Development of the universal and simplified soil model coupling heat and water transport. *Sci. China Ser. D Earth Sci.* 51, 88–102. <https://doi.org/10.1007/s11430-007-0153-2>.
- Li, J., Sheng, Y., Wu, J., Feng, Z., Ning, Z., Hu, X., Zhang, X., 2016a. Mapping frozen soil distribution and modeling permafrost stability in the source area of the Yellow River. *Sci. Geogr. Sin.* 36.
- Li, J., Sheng, Y., Wu, J., Feng, Z., Wang, S., Cao, Y., Hu, X., Cao, W., Wang, J., Zhang, X., 2016b. Variations in the ground temperatures of permafrost in the two watersheds of the

- interior and eastern Qilian Mountains. *Environ. Earth Sci.* 75, 480. <https://doi.org/10.1007/s12665-016-5330-1>.
- LIGG/CAS, 1995. Remote Sensing Map for Frozen Ground of the West Route of South-to-North Water Transfer Project-Tongtian to Yalong Rivers Transfer Region (1:500000).
- Lin, L., Jin, H., Luo, D., Lv, L., He, R., 2014. Preliminary study on major features of alpine vegetation in the Source Area of the Yellow River (SAYR). *J. Glaciol. Geocryol.* 36, 230–236. <https://doi.org/10.7522/j.issn.1000-0240.2014.0029>.
- Ling, F., Wu, Q., Zhang, T., Niu, F., 2012. Modelling open-talik formation and permafrost lateral thaw under a thermokarst lake, Beiluhe Basin, Qinghai-Tibet Plateau. *Permaf. Periglac. Process.* 23, 312–321. <https://doi.org/10.1002/ppp.1754>.
- Liu, Y., Jiang, D., 2016. Last glacial maximum permafrost in China from CMIP5 simulations. *Palaeogeogr. Palaeoclimatol. Palaeoecol.* 447, 12–21. <https://doi.org/10.1016/j.palaeo.2016.01.042>.
- Liu, J., Liu, M., Zhuang, D., Zhang, Z., Deng, X., 2003. Study on spatial pattern of land-use change in China during 1995–2000. *Sci. China Ser. D Earth Sci.* 46, 373–384. <https://doi.org/10.1360/03yd9033>.
- Lugon, R., Monbaron, M., 1998. Stabilité des terrains meubles en zone de pergélisol et changements climatiques. Deux études de cas en Valais: le Ritigraben (Mattertal) et la moraine du Dolent (Val Ferret). *Hochschulverlag AG an der ETH Zurich, Zurich*.
- Luo, D., Jin, H., Lin, L., He, R., Yang, S., Chang, X., 2012. New progress on permafrost temperature and thickness in the source area of the Huanghe River. *Sci. Geogr. Sin.* 32, 898–904.
- Luo, D., Jin, H., Lin, L., You, Y., Yang, S., Wang, Y., 2013. Distributive features and controlling factors of permafrost and the active layer thickness in the Bayan Har Mountains along the Qinghai-Kangding Highway on northeastern Qinghai-Tibet Plateau. *Sci. Geogr. Sin.* 33, 635–640.
- Luo, D., Jin, H., Lv, L., Wu, Q., 2014a. Spatiotemporal characteristics of freezing and thawing of the active layer in the source areas of the Yellow River (SAYR). *Chin. Sci. Bull.* 59, 3034–3045. <https://doi.org/10.1007/s11434-014-0189-6>.
- Luo, D., Jin, H., Marchenko, S., Romanovsky, V., 2014b. Distribution and changes of active layer thickness (ALT) and soil temperature (TTOP) in the source area of the Yellow River using the GIPL model. *Sci. China Earth Sci.* 57, 1834–1845.
- Marchenko, S., 2008. Numerical Modeling of Spatial Permafrost Dynamics in Alaska. Presented at the Ninth International Conference on Permafrost, Sheridan Press, Fairbanks, pp. 1125–1130 <https://doi.org/10.5194/tc-6-613-2012>.
- McKenzie, J.M., Voss, C.I., 2013. Permafrost thaw in a nested groundwater-flow system. *Hydrogeol. J.* 21, 299–316. <https://doi.org/10.1007/s10040-012-0942-3>.
- Nan, Z., Li, S., Liu, Y., 2002. Mean annual ground temperature distribution on the Tibetan Plateau: permafrost distribution mapping and further application. *J. Glaciol. Geocryol.* 24, 142–148.
- Nan, Z., Li, S., Cheng, G., 2005. Prediction of permafrost distribution on the Qinghai-Tibet Plateau in the next 50 and 100 years. *Sci. China Ser. D Earth Sci.* 48, 797–804. <https://doi.org/10.1360/03yd0258>.
- Nelson, F.E., Anisimov, O.A., Shiklomanov, N.I., 2001. Subsidence risk from thawing permafrost. *Nature* 410, 889–890. <https://doi.org/10.1038/35073746>.
- Ni, J., 2000. A simulation of biomes on the Tibetan Plateau and their responses to global climate change. *Mt. Res. Dev.* 20, 80–89. [https://doi.org/10.1659/0276-4741\(2000\)020\[0080:ASOBOT\]2.0.CO;2](https://doi.org/10.1659/0276-4741(2000)020[0080:ASOBOT]2.0.CO;2).
- Nicolsky, D.J., Romanovsky, V.E., Panda, S.K., Marchenko, S.S., Muskett, R.R., 2017. Applicability of the ecosystem type approach to model permafrost dynamics across the Alaska North Slope. *J. Geophys. Res. Earth Surf.* 122, 50–75. <https://doi.org/10.1002/2016JF003852>.
- Noetzel, J., Gruber, S., Kohl, T., Salzmann, N., Haeblerli, W., 2007. Three-dimensional distribution and evolution of permafrost temperatures in idealized high-mountain topography. *J. Geophys. Res.* 112 <https://doi.org/10.1029/2006JF000545>.
- Ollesch, G., Kistner, I., Meissner, R., Lindenschmidt, K.-E., 2006. Modelling of snowmelt erosion and sediment yield in a small low-mountain catchment in Germany. *Catena* 68, 161–176. <https://doi.org/10.1016/j.catena.2006.04.005> (Soil Erosion Research in Europe).
- Painter, S.L., Coon, E.T., Atchley, A.L., Berndt, M., Garimella, R., Moulton, J.D., Svyatskiy, D., Wilson, C.J., 2016. Integrated surface/subsurface permafrost thermal hydrology: model formulation and proof-of-concept simulations. *Water Resour. Res.* 52, 6062–6077. <https://doi.org/10.1002/2015WR018427>.
- Pan, B., Li, J., 1996. Qinghai-Tibetan Plateau: a driver and amplifier of global climate changes-3 the effects of the uplift of Qinghai-Tibetan Plateau on climate changes. *J. Lanzhou Univ. (Nat. Sci.)* 32, 108–115.
- Pan, B., Li, J., Chen, F., 1995a. Qinghai-Tibetan Plateau: a driver and amplifier of global climate changes-1 basic characteristics of climate changes in Cenozoic Era. *J. Lanzhou Univ. (Nat. Sci.)* 31, 120–128.
- Pan, B., Li, J., Zhu, J., Cao, J., 1995b. Qinghai-Tibetan Plateau: a driver and amplifier of global climate changes-2 uplift process of the Qinghai-Xizang (Tibetan) Plateau. *J. Lanzhou Univ. (Nat. Sci.)* 31, 160–167.
- Qin, Y., Yang, D., Gao, B., Wang, T., Chen, J., Chen, Y., Wang, Y., Zheng, G., 2017. Impacts of climate warming on the frozen ground and eco-hydrology in the Yellow River source region, China. *Sci. Total Environ.* 605, 830–841. <https://doi.org/10.1016/j.scitotenv.2017.06.188>.
- Ran, Y., Li, X., Cheng, G., Zhang, T., Wu, Q., Jin, H., Jin, R., 2012. Distribution of permafrost in China: an overview of existing permafrost maps. *Permaf. Periglac. Process.* 23, 322–333. <https://doi.org/10.1002/ppp.1756>.
- Riseborough, D., Shiklomanov, N., Etzelmueller, B., Gruber, S., Marchenko, S., 2008. Recent advances in permafrost modelling. *Permaf. Periglac. Process.* 19, 137–156. <https://doi.org/10.1002/ppp.615>.
- Romanovsky, V.E., Smith, S.L., Christiansen, H.H., 2010. Permafrost thermal state in the polar northern hemisphere during the international polar year 2007–2009: a synthesis. *Permaf. Periglac. Process.* 21, 106–116. <https://doi.org/10.1002/ppp.689>.
- Schulla, J., Jasper, K., 2015. Modell Description WaSiM (Water Balance Simulation Model). Shangguan, W., Hengl, T., Mendes de Jesus, J., Yuan, H., Dai, Y., 2017. Mapping the global depth to bedrock for land surface modeling. *J. Adv. Model. Earth Syst.* 9, 65–88. <https://doi.org/10.1002/2016MS000686>.
- Sheng, Y., Cao, Y., Li, J., Wu, J., Chen, J., Feng, Z., 2015. Characteristics of permafrost along highway G214 in the eastern Qinghai-Tibet Plateau. *J. Mt. Sci.* 12, 1135–1144. <https://doi.org/10.1007/s11629-014-3207-x>.
- Shi, Y., Mi, D., 1988. Map of Snow, Ice and Frozen Ground in China.
- Shi, X.Z., Yu, D.S., Warner, E.D., Pan, X.Z., Petersen, G.W., Gong, Z.G., Weindorf, D.C., 2004. Soil database of 1:1,000,000 digital soil survey and reference system of the Chinese genetic soil classification system. *Soil Horiz.* 45, 129–136. <https://doi.org/10.2136/sh2004.4.0129>.
- Smith, M.W., Riseborough, D.W., 1996. Permafrost monitoring and detection of climate change. *Permaf. Periglac. Process.* 7, 301–309. [https://doi.org/10.1002/\(SICI\)1099-1530\(199610\)7:4<301::AID-PPP231>3.0.CO;2-R](https://doi.org/10.1002/(SICI)1099-1530(199610)7:4<301::AID-PPP231>3.0.CO;2-R).
- Stahl, K., Moore, R.D., Floyer, J.A., Asplin, M.G., McKendry, I.G., 2006. Comparison of approaches for spatial interpolation of daily air temperature in a large region with complex topography and highly variable station density. *Agric. For. Meteorol.* 139, 224–236. <https://doi.org/10.1016/j.agrformet.2006.07.004>.
- Stocker, T.F., Qin, D., Plattner, G.K., Tignor, M.M.B., Allen, S.K., Boschung, J., Nauels, A., Xia, Y., Bex, V., Midgley, P.M., 2013. Climate Change 2013: The Physical Science Basis. Contribution of Working Group I to the Fifth Assessment Report of IPCC the Intergovernmental Panel on Climate Change.
- Su, J.J., van Bochove, E., Thériault, G., Novotna, B., Khaldoune, J., Denault, J.T., Zhou, J., Nolin, M.C., Hu, C.X., Bernier, M., Benoy, G., Xing, Z.S., Chow, L., 2011. Effects of snowmelt on phosphorus and sediment losses from agricultural watersheds in Eastern Canada. *Agric. Water Manag.* 98, 867–876. <https://doi.org/10.1016/j.agwat.2010.12.013>.
- Sun, L., Zhao, L., Li, R., Yao, J., Xiao, Y., Liu, G., 2010. The influence of snow cover on the surface albedo and ground temperature. *J. Mt. Sci.* 28, 266–273. <https://doi.org/10.16089/j.cnki.1008-2786.2010.03.005>.
- Tian, D., Guo, Y., Dong, W., 2015. Future changes and uncertainties in temperature and precipitation over China based on CMIP5 models. *Adv. Atmos. Sci.* 32, 487–496. <https://doi.org/10.1007/s00376-014-4102-7>.
- Walvoord, M.A., Kurylyk, B.L., 2016. Hydrologic impacts of thawing permafrost—a review. *Vadose Zone J.* 15. <https://doi.org/10.2136/vzj2016.01.0010>.
- Walvoord, M.A., Voss, C.I., Wellman, T.P., 2012. Influence of permafrost distribution on groundwater flow in the context of climate-driven permafrost thaw: example from Yukon Flats Basin, Alaska, United States. *Water Resour. Res.* 48, W07524. <https://doi.org/10.1029/2011WR011595>.
- Wang, T., 2006. 1:4000000 Map of the Glaciers, Frozen Ground and Deserts in China.
- Wang, W., Cheng, G., 2001. Characteristics of grassland and ecological changes of vegetation in the source regions of Yangtze and Yellow Rivers. *J. Desert Res.* 21, 101–107.
- Wang, Q., Zhou, L., 1998. Diagnostic analysis of climatic changes in source region of Yellow River and Yangtze River. *Qinghai Environ.* 8, 73–77.
- Wang, G., Shen, Y., Cheng, G., 2000. Eco-environmental changes and causal analysis in the source regions of the Yellow River. *J. Glaciol. Geocryol.* 22, 200–205.
- Wang, L., Koike, T., Yang, K., Jin, R., Li, H., 2010. Frozen soil parameterization in a distributed biosphere hydrological model. *Hydrol. Earth Syst. Sci.* 14, 557–571. <https://doi.org/10.5194/hess-14-557-2010>.
- Wang, S., Sheng, Y., Wu, J., Li, J., Chen, J., 2015. The characteristics and changing tendency of permafrost in the source regions of the Datong River, Qilian Mountains. *J. Glaciol. Geocryol.* 37, 27–37.
- Wang, T., Yang, D., Qin, Y., Wang, Y., Chen, Y., Gao, B., Yang, H., 2018. Historical and future changes of frozen ground in the upper Yellow River Basin. *Glob. Planet. Chang.* 162, 199–211. <https://doi.org/10.1016/j.gloplacha.2018.01.009>.
- Wang, T., Yang, D., Fang, B., Yang, W., Qin, Y., Wang, Y., 2019. Data-driven mapping of the spatial distribution and potential changes of frozen ground over the Tibetan Plateau. *Sci. Total Environ.* 649, 515–525. <https://doi.org/10.1016/j.scitotenv.2018.08.369>.
- Warscher, M., Strasser, U., Kraller, G., Marke, T., Franz, H., Kunstmann, H., 2013. Performance of complex snow cover descriptions in a distributed hydrological model system: a case study for the high Alpine terrain of the Berchtesgaden Alps. *Water Resour. Res.* 49, 2619–2637. <https://doi.org/10.1002/wrcr.20219>.
- Williams, S.F., 2010. The Coordinated Energy and Water Cycle Observations Project (CEOP) Data Integration Approach. Presented at the 10th EMS Annual Meeting, 10th European Conference on Applications of Meteorology (ECAM) Abstracts, Zürich, Switzerland (pp. EMS2010-798).
- Wu, Q., Zhang, T., 2008. Recent permafrost warming on the Qinghai-Tibetan Plateau. *J. Geophys. Res.-Atmos.* 113. <https://doi.org/10.1029/2007JD009539>.
- Wu, Q., Zhang, T., 2010. Changes in active layer thickness over the Qinghai-Tibetan Plateau from 1995 to 2007. *J. Geophys. Res.-Atmos.* 115, D09107. <https://doi.org/10.1029/2009JD012974>.
- Wu, Q., Lu, Z., Liu, Y., 2005. Permafrost monitoring and its recent changes in Qinghai-Tibet Plateau. *Adv. Clim. Chang. Res.* 1, 26–28.
- Wu, Q., Zhang, T., Liu, Y., 2010. Permafrost temperatures and thickness on the Qinghai-Tibet Plateau. *Glob. Planet. Chang.* 72, 32–38. <https://doi.org/10.1016/j.gloplacha.2010.03.001>.
- Yang, J., Ding, Y., Shen, Y., Liu, S., Chen, R., 2004. Climatic features of eco-environment change in the source regions of the Yangtze and Yellow Rivers in recent 40 years. *J. Glaciol. Geocryol.* 26, 7–16.
- Yang, J., Yang, S., Li, M., Tan, C., 2013. Vulnerability of frozen ground to climate change in China. *J. Glaciol. Geocryol.* 35, 1436–1445. <https://doi.org/10.7522/j.issn.1000-0240.2013.0159>.
- Zeng, Y., Feng, Z., 2007. Spatial and temporal changes of desertification in the headwater area of the Yellow River using remote sensing. *Acta Geograph. Sin.* 62, 529–536.
- Zhang, T., Starnes, K., 1998. Impact of climatic factors on the active layer and permafrost at Barrow, Alaska. *Permaf. Periglac. Process.* 9, 229–246. [https://doi.org/10.1002/\(SICI\)1099-1530\(199807\)9:3<229::AID-PPP286>3.0.CO;2-T](https://doi.org/10.1002/(SICI)1099-1530(199807)9:3<229::AID-PPP286>3.0.CO;2-T).

- Zhang, Z., Wu, Q., 2012. Prediction changes of active layer thickness on the Qinghai-Tibet Plateau as climate warming. *J. Glaciol. Geocryol.* 34, 505–511.
- Zhang, T., Osterkamp, T.E., Stamnes, K., 1996. Influence of the depth hoar layer of the seasonal snow cover on the ground thermal regime. *Water Resour. Res.* 32, 2075–2086. <https://doi.org/10.1029/96WR00996>.
- Zhang, Y., Chen, W., Riseborough, D.W., 2006a. Temporal and spatial changes of permafrost in Canada since the end of the Little Ice Age. *J. Geophys. Res.-Atmos.* 111. <https://doi.org/10.1029/2006JD007284>.
- Zhang, Y., Liu, L., Bai, W., Shen, Z., Yan, J., Ding, M., Li, S., Zheng, D., 2006b. Grassland degradation in the source region of the Yellow River. *Acta Geograph. Sin.* 61, 3–14.
- Zhang, Y., Chen, W., Riseborough, D.W., 2008. Transient projections of permafrost distribution in Canada during the 21st century under scenarios of climate change. *Glob. Planet. Chang.* 60, 443–456. <https://doi.org/10.1016/j.gloplacha.2007.05.003>.
- Zhang, Y., Cheng, G., Li, X., Han, X., Wang, L., Li, H., Chang, X., Flerchinger, G.N., 2013a. Coupling of a simultaneous heat and water model with a distributed hydrological model and evaluation of the combined model in a cold region watershed. *Hydrol. Process.* 27, 3762–3776. <https://doi.org/10.1002/hyp.9514>.
- Zhang, Y., Wang, X., Fraser, R., Olthof, I., Chen, W., Mclennan, D., Ponomarenko, S., Wu, W., 2013b. Modelling and mapping climate change impacts on permafrost at high spatial resolution for an Arctic region with complex terrain. *Cryosphere* 7. <https://doi.org/10.5194/tc-7-1121-2013>.
- Zhao, S., Nan, Z., Huang, Y., Zhao, L., 2017. The application and evaluation of simple permafrost distribution models on the Qinghai-Tibet Plateau. *Permafr. Periglac. Process.* 28, 391–404. <https://doi.org/10.1002/ppp.1939>.
- Zhou, Y., Guo, D., Qiu, G., Cheng, G., Li, S., 2000. *Geocryology in China*.